Accepted refereed manuscript of:

Wijeakumar S, Huppert TJ, Magnotta VA, Buss AT & Spencer JP (2017) Validating an image-based fNIRS approach with fMRI and a working memory task, *NeuroImage*, 147, pp. 204-218..

DOI: 10.1016/j.neuroimage.2016.12.007

Validating an image-based fNIRS approach with fMRI and a working memory task.

Sobanawartiny Wijeakumar[a], Theodore Huppert[b], Vincent A. Magnotta[c], Aaron T. Buss[d] & John P. Spencer[a]

a. School of Psychology, University of East Anglia, Norwich, NR4 7TJ
b. Department of Radiology, University of Pittsburgh, Pittsburgh PA 15213
c. University of Iowa, Department of Radiology and Delta Center, Iowa City 52242, Iowa, U.S.A
d. University of Tennessee, Department of Psychology, Knoxville, Tennessee 37996, U.S.A

Corresponding authors

Sobanawartiny Wijeakumar
Senior Research Associate
School of Psychology
University of East Anglia
Norwich
NR4 7TJ
United Kingdom
Email: S.Wijeakumar@uea.ac.uk
Phone number: 0044-07385397211

John P. Spencer
Professor
School of Psychology
University of East Anglia
Norwich
NR4 7TJ
United Kingdom
Email: j.spencer@uea.ac.uk

Abstract

In the current study, we extend a previous methodological pipeline by adding a novel image reconstruction approach to move functional near-infrared (fNIRS) signals from channel-space on the surface of the head to voxel-space within the brain volume. We validate this methodology by comparing voxel-wise fNIRS results to functional magnetic resonance imaging (fMRI) results from a visual working memory (VWM) task using two approaches. In the first approach, significant voxel-wise correlations were observed between fNIRS and fMRI measures for all experimental conditions across brain regions in the fronto-parieto-temporal cortices. In the second approach, we conducted separate multi-factorial ANOVAs on fNIRS and fMRI measures and then examined the correspondence between main and interaction effects within common regions of interest. Both fMRI and fNIRS showed similar trends in activation within the VWM network when the number of items held in working memory increases. These results validate the image-based fNIRS approach.

Keywords

Functional near-infrared spectroscopy

Functional magnetic resonance imaging

Visual working memory

Image reconstruction

Working memory load

Highlights

- Novel image reconstruction technique was validated by simultaneously measuring brain activity with fNIRS and fMRI.
- Both modalities show positive and negative correlations across visual working memory conditions.
- Both modalities show similar trends in activation in response to increases in working memory load.

1. Introduction

Functional magnetic resonance imaging is widely considered to be the gold standard for neuroimaging. It provides excellent spatial resolution that has proven useful in a variety of clinical and non-clinical applications. Nevertheless, fMRI has limitations. It does not provide good temporal resolution and there is debate about the origin and nature of the blood oxygen-level dependent signal (BOLD) (Logothetis N.K. Augath M., Trinath T., Oeltermann A, 2001). It is also difficult to use fMRI with infants, children, and some clinical and aging populations because participants need to lie still in the scanner. Finally, fMRI cannot be used to scan people who have 'movable' metal fragments in their body.

An alternative neuroimaging technique that overcomes some of these limitations is functional near infrared spectroscopy (fNIRS) (Boas et al., 2014; Ferrari and Quaresima, 2012). fNIRS systems shine near-infrared light at two or more different wavelengths through brain tissue. The two wavelengths of light are differentially absorbed by oxy (HbO) and de-oxy hemoglobin (HbR). Based on this, a localized measure of HbO and HbR concentration in the underlying brain tissue can be determined. Thus, fNIRS provides independent measurements of both chromophores; this has the potential to reveal new insights into neurovascular coupling, particularly given the high temporal resolution of fNIRS. fNIRS can be used with neonates, children, and atypical populations because it is relatively more resistant to motion artifacts. Further, the presence of movable metal fragments is not a limitation with fNIRS. For these reasons, fNIRS has become a neuroimaging tool of choice for these populations. The primary limitation of fNIRS is its poorer spatial resolution relative to fMRI. High quality fNIRS signals can only be obtained from approximately the outer centimeter of cortical tissue. Although this prevents recording from deeper parts of the brain, the spatial resolution obtained in the outer brain tissue is better than that provided by EEG.

fNIRS has been widely used to investigate visual, auditory, motor and cognitive stimulation both in non-clinical and clinical settings (Boas et al., 2014;

Bortfeld et al., 2009, 2007; Brigadoi et al., 2012; Wijeakumar et al., 2012a, 2012b). The use of fNIRS in these areas has been spurred forward by validation studies using simultaneous fMRI and fNIRS (Cui et al., 2011; Emir et al., 2008; Erdoğan et al., 2014; Fabiani et al., 2014; Huppert et al., 2006, 2005; Maggioni et al., 2015; Muthalib et al., 2013; Okamoto et al., 2004; Pflieger and Barbour, 2012; Sakatani et al., 2013; Sassaroli et al., 2005; Sato et al., 2013; Steinbrink et al., 2006; Strangman et al., 2002; Tong and Frederick, 2012; Yücel et al., 2012). These studies have demonstrated good spatial and temporal correlation between both techniques, primarily using tasks that engage the sensorimotor cortices (e.g., finger tapping tasks). Given the increasing number of studies using fNIRS to understand cognition, it is important to validate the use of fNIRS using cognitive tasks to establish whether the correlation between fMRI and fNIRS measures holds beyond the sensorimotor cortex.

One cognitive system that has been extensively studied across the lifespan with functional neuroimaging is visual working memory (VWM). VWM is an important cognitive system that accounts for up to 43% of individual differences in global fluid intelligence (Luck and Vogel, 2013). Previous fMRI studies have identified a fronto-parieto-temporal network (Druzgal and D'Esposito, 2003; Learmonth et al., 2001; Linden et al., 2003; Ma et al., 2014; Pessoa and Ungerleider, 2004; Postle, 2015; Rypma et al., 2002; Todd & Marois, R., 2005; Todd and Marois, 2004) that is engaged in VWM tasks as well as parts of this network that are differentially activated by parametric manipulations of, for instance, the working memory load (Todd and Marois, 2004). Most regions in this network fall within the cortical depth measured by fNIRS; thus, VWM is a good target for validating the use of fNIRS in cognitive applications (Cui et al., 2011; Cutini et al., 2011; Fishburn et al., 2014; McKendrick et al., 2014; Molteni et al., 2008; Ogawa et al., 2014; Perlman et al., 2015; Tanaka et al., 2014). To date, two validation studies have correlated fMRI and fNIRS measures in VWM tasks (Cui et al., 2011; Sato et al., 2013). Here, we extend these previous efforts by validating a novel image reconstruction approach to fNIRS data.

A central challenge when using fNIRS is that the sensors are placed on the surface of the head, but the questions of interest are about localized activity within the brain volume. Standard fNIRS analysis approaches treat each channel as independent, and significant channel-based effects are often discussed with reference to the 10-20 system of electrode placement. This has several limitations. First, it is difficult to precisely align an fNIRS probe across participants' heads due to variations in head size and shape (Tsuzuki and Dan, 2014). For instance, many studies place the optical probes within a rigid body that is then affixed to the head at a particular reference point in the 10-20 system. Although this places the probe over the correct cortical region, slight rotations of the rigid body on the head can create variations in which cortical regions are measured across participants. This challenge is exacerbated with infants, young children, and clinical populations who have difficulty sitting still.

Second, by treating each fNIRS channel as independent, researchers fail to capitalize on cases where channels record from overlapping regions of cortex. In such cases, weak effects that live at the intersection of channels might not be detected in channel-based analysis. Third, channel-based analyses make it difficult to compare results across studies and to findings from fMRI studies. It would be ideal if we could, for instance, determine whether an effect reported in an fNIRS study was localized in the same region of cortex as a related effect measured with fMRI. Finally, to date, analytic tools developed in the fNIRS literature are often isolated from analytic tools developed in the fMRI literature and vice versa.

One potential solution would be to transform channel-based time-domain fNIRS signals into voxel-based fNIRS activation maps, similar to those reported in fMRI studies. Perlman et al. (2015) used an image reconstruction approach to study activation in response to a VWM task in 3- to 7-year-olds that was based on work by Boas, Culver, and colleagues (Fang and Boas, 2009; Perlman et al., 2015). Here, we build on this and related work (Brigadoi et al., 2015) and ask whether this image reconstruction approach identifies similar clusters of task-related activation within the brain volume measured with simultaneous fMRI.

In the sections that follow, we describe the image reconstruction approach. The pipeline we developed builds on a set of methodological tools that help with the design of fNIRS probe geometries (Wijeakumar et al., 2015). Here, we extend these tools, adding a novel image reconstruction approach to move fNIRS signals from channel-space to voxel-space. We then attempt to validate this approach by examining the correspondence between fMRI and image-based fNIRS in response to a VWM task that we adapted from work by Todd and Marois (2004). First, we examine correlations between HbO and HbR and BOLD activation maps. In a second validation step, we look at whether parametric effects measured with fMRI were also evident in the image-based fNIRS results. An important neural signature that has emerged from the fMRI VWM literature is the increase and gradual asymptote in neural activation levels as the working memory load is increased. In the current study, we will hone in on exemplar clusters that show an effect of working memory load and demonstrate that both fNIRS and fMRI show similar trends in activation levels.

2. Materials and Methods

2.1. Subjects

Thirteen (6 Males; M age = 25.7; SD = 4.2) native English-speaking participants completed the fMRI-fNIRS study. All of them were students at the University of Iowa. All participants had normal or corrected-to-normal vision and signed an informed consent form approved by the Ethics Committee at the University of Iowa.

2.2. Stimuli and Task Design

We used a Change Detection task. The experimental paradigm was created using E-prime version 2.0 and was run on an HP computer (Windows 7).

Each trial began with a verbal load of two aurally presented letters; see (Todd and Marois, 2004). At the end of each trial, participants were asked to repeat the presented letters to eliminate the possibility of verbal rehearsal of the colors of the stimuli. Following the presentation of the letters, a Sample array of colored squares (24 x 24 pixels) was presented for 500 ms (randomly sampled

from CIE*Lab color-space at least 60° apart). Squares were randomly spaced at least 30° apart along an imaginary circle (100 pixels). The Sample array was followed by a delay of 1200 ms. The delay was followed by the Test array for 1800 ms. The Test array was presented with the same number of colored squares as the Sample array, but the Test array could either match the colors of the Sample array ('Same' trials) or the color of a randomly-selected square was shifted 36° in color space ('Different' trials). Participants had to indicate with a button press if the Test array matched the Sample array.

Working memory load was manipulated such that two (Load 2), four (Load 4) or six (Load 6) squares were presented during the Sample and Test arrays. Participants completed five runs of 120 trials (3 runs at Load 4; 1 run each of Load 2, Load 6) in one of two orders (Load 2, Load 4, Load 6, Load 4, Load 4 or Load 6, Load 4, Load 2, Load 4, Load 4). Three out of thirteen participants did not complete all three runs of Load 4 due to the discomfort of lying in the scanner with the fNIRS sensors attached.

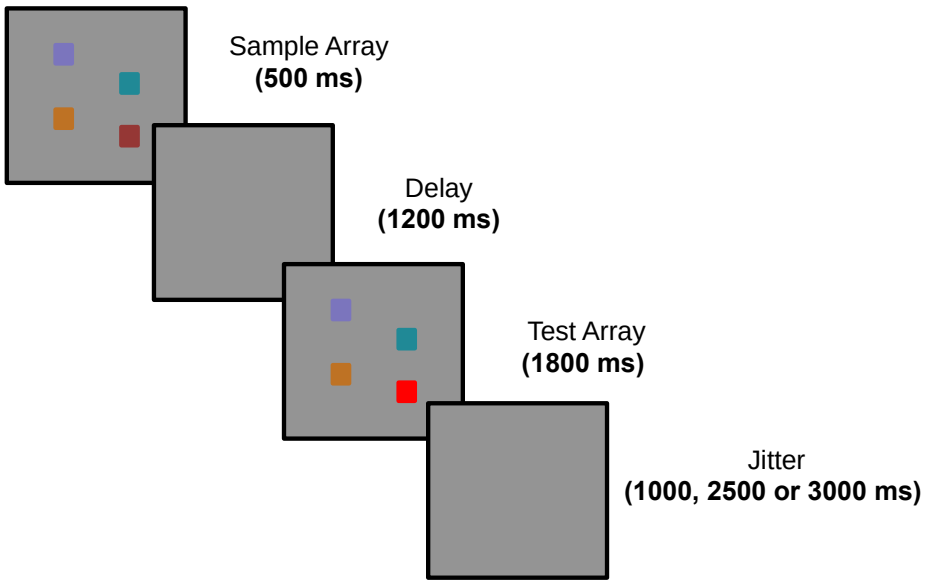

Figure 1. Change detection paradigm.

2.3. fNIRS Acquisition

A 24-channel TechEn CW6 (12 sources and 24 detectors) system with wavelengths of 830 nm and 690 nm was used to collect fNIRS data at 25 Hz

simultaneously with fMRI data collection. Fiber optic cables were used to deliver light to a customized cap designed for use within the MRI scanner. The cap consisted of channels in 6 arrays covering the left and right frontal, temporal, and parietal regions. Each array consisted of two sources and four detectors. The arrays overlying the frontal and parietal cortices had five channels each with 3 cm source-detector (SD) separation and two channels with 1 cm SD separation. The arrays overlying the temporal cortex consisted of four channels with 3 cm SD separation and two channels with 1 cm SD (short source-detector channels) separation. In total, the probe had 40 channels. These arrays were placed on the head relative to the 10–20 system. Note that only six out of the thirteen participants had usable data from the short source-detector channels. Therefore, we did not include data from the short source-detector channels for any of the participants in our analyses. Consequently, we ended up with 28 channels per participant (see Figure 2a). Vitamin E capsules were placed on the fNIRS probe so that the positions of the channels could be detected on the structural scans.

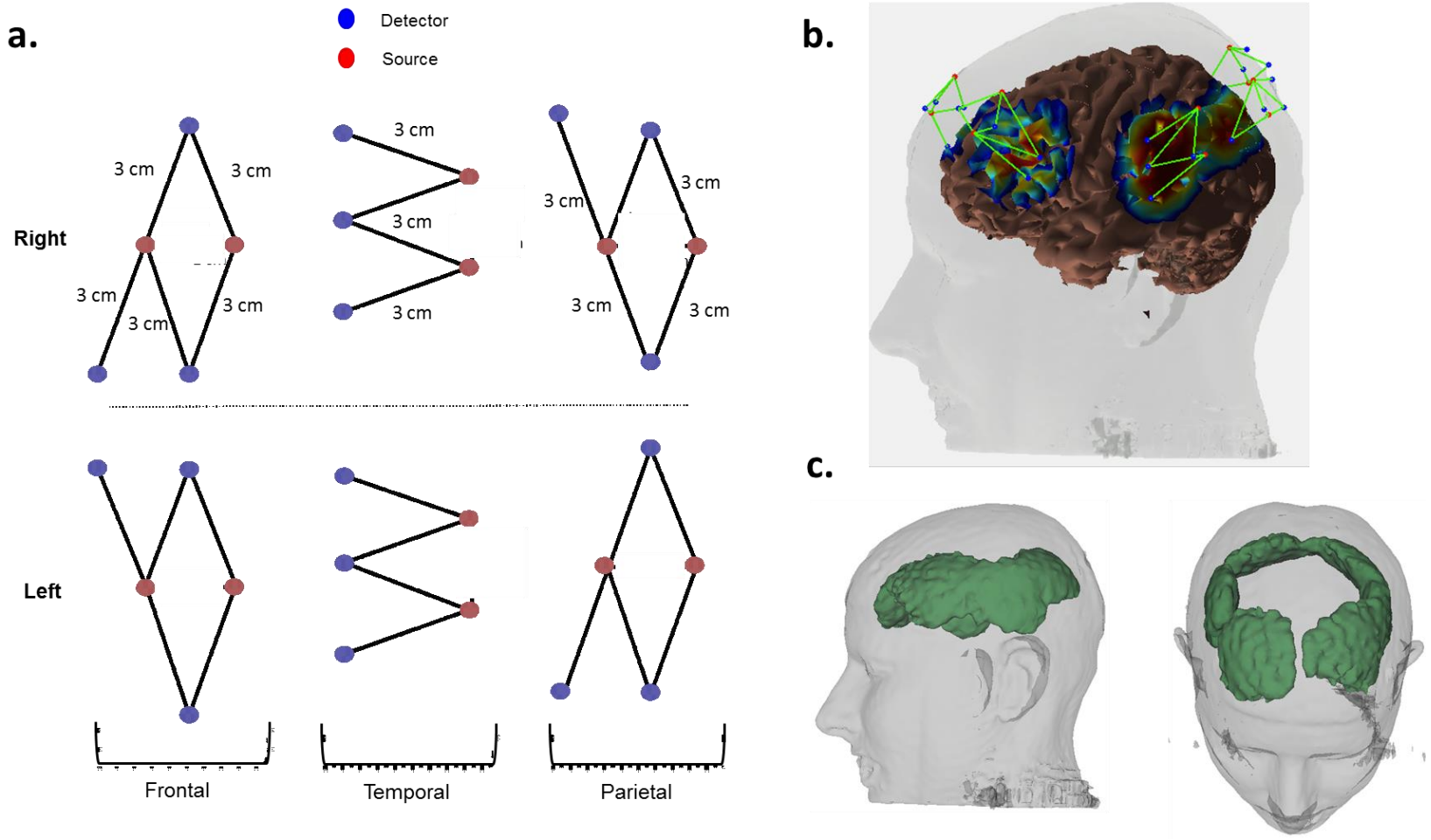

Figure 2 (a) Probe geometry covering the frontal, temporal and parietal cortices. (b) Left hemispheric view of the optodes projected onto a single subject's head (segmented atlas from MRI scan). Red and blue dots represent sources and detectors and the green lines show respective channels. (c) 3D representation of the intersected fNIRS-fMRI mask computed across participants.

227 2.4 fNIRS Processing (Steps 1-2 in Figure 3)

228 Figure 3 shows a flowchart of the processing pipeline. The steps shown in
229 the flowchart are discussed in the following sections.

230 fNIRS data were preprocessed using HOMER2
231 (www.nmr.mgh.harvard.edu/PMI/resources/homer2). Raw data were converted
232 to optical density units. Targeted principal components analysis (AMPThresh =
233 0.5, STDthresh = 50, tMask = 1, and tMotion = 1) was applied to the data to
234 identify and correct motion artifacts (Yücel et al., 2014). The data were then
235 screened for residual motion using motion artifact correction (using the same
236 parameters as above) and those trials that did not meet the criteria were
237 excluded from further analysis. No trials were lost due to motion (there was little
238 motion since participants had to lie still inside the MRI head coil). Data were
239 band-pass filtered (0.016 – 0.5 Hz) to remove low frequency drifts and high
240 frequency noise. Data were then converted to HbO and HbR concentration units
241 using the modified Beer-Lambert Law.

242 Channel-based weighted block averages (used in the majority of previous
243 fNIRS studies) computed across all participants for the Hit condition showed
244 evidence for increasing HbO concentration with increasing working memory load
245 in some channels (see channels 3, 8, 9, 14, 15, 18, 19 and 20 in Supplementary
246 Figure 2). Channel-based weighted block averages for HbR activation have been
247 shown in Supplemental Figure 3. Critically, however, there is limited information
248 about the spatial distribution of these results. Further, in this state, results cannot
249 be directly compared to voxel-based results that fMRI studies yield. To examine
250 these issues, we need to translate these channel-based results to voxel-space
251 using image reconstruction methods. *Note that these conventional channel-*
252 *based block averages are for illustration purposes only; these averages were not*
253 *used below. Rather, the pipeline we developed uses a general linear modeling*
254 *approach that capitalizes on the event-related nature of the experimental design.*

255 To analyze the fNIRS data, a general linear model with 12 regressors was
256 conducted on the HbO and HbR data. The 12 regressors consisted of correct
257 responses on different trials (Hits), correct responses on same trials (CR),

incorrect responses on different trials (Miss), and incorrect responses on same trials (FA) for each of the Load 2, Load 4, and Load 6 runs (4 trial types x 3 loads = 12 regressors). Regressors were created by convolving the onset of the Sample array for each of the conditions with a canonical single parameter gamma variate function. Consequently, we obtained a beta coefficient for each condition, channel, chromophore, and participant.

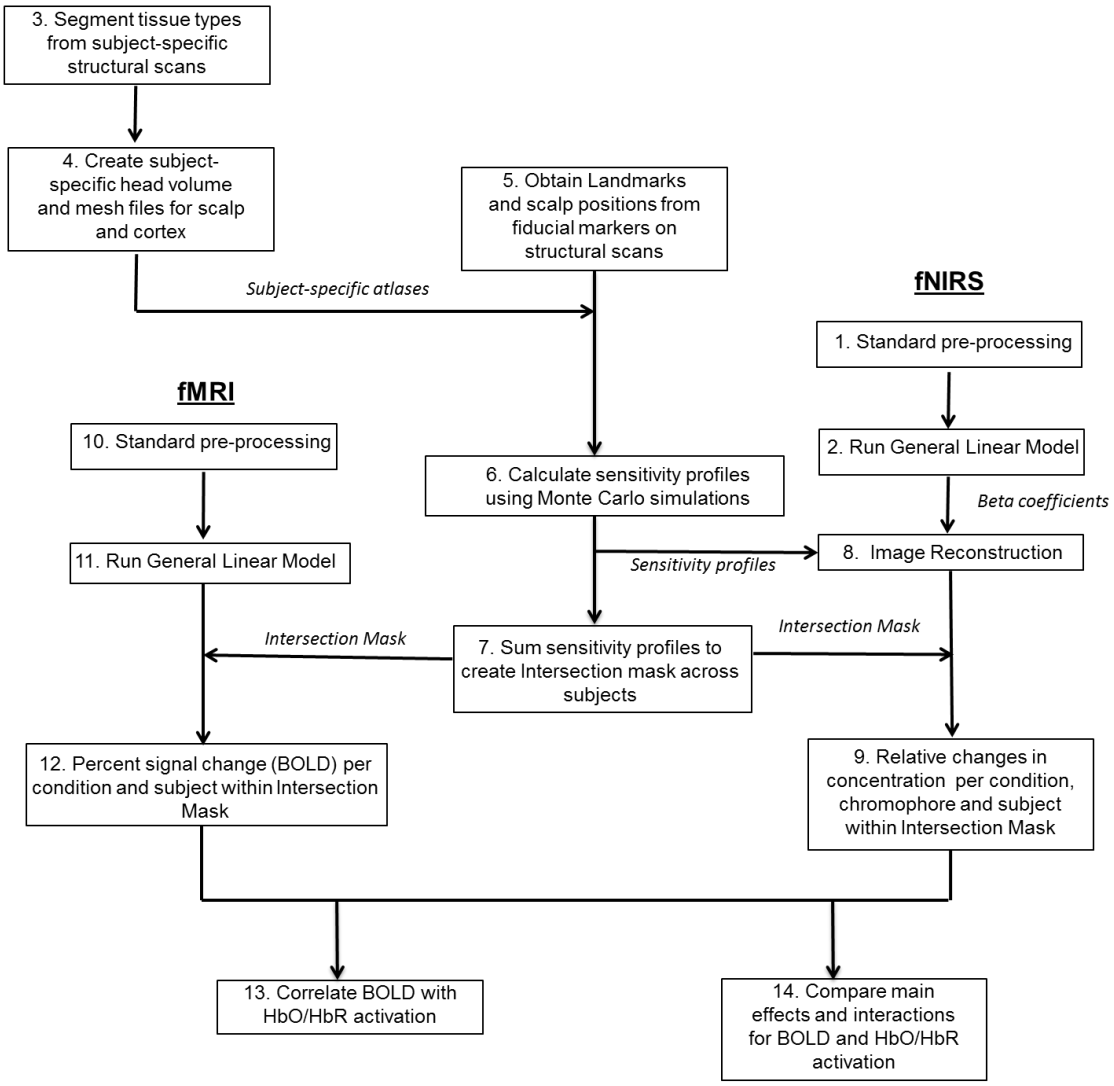

Figure 3. Flowchart of the processing pipeline

Figure 3. Weighted block average HbO signals for Hit trials for Loads 2 (shown in blue), 4 (shown in green) and 6 (shown in red) across the frontal (outlined in red), temporal (outlined in green) an and parietal (outlined in blue) channels.

2.5. Monte Carlo Simulations (Steps 3-7 in Figure 3)

Each participant's structural scan was segmented using *3dSeg* into separate volumes for gray matter, white matter, cerebro-spinal fluid, and scalp tissue. These tissue volumes were identified and assigned unique values. These volumes were then converted to 3D mesh surfaces and merged together to create a subject-specific head atlas using scripts in the *HOMER2* repository (Wijeakumar et al., 2015). We chose to use subject-specific structural scans instead of a generic adult atlas following findings from Cooper and colleagues (Cooper et al., 2012). They reported that the Euclidean error in localization with reference to a center of activation increased two-fold when an atlas was used instead of a segmented atlas from the individual's MRI scan.

Slicer3D was used to visualize and then extract the scalp landmarks and positions of sources and detectors from Vitamin E capsules placed on the structural scans of the participants. *AtlasViewerGUI* (available within HOMER2: www.nmr.mgh.harvard.edu/PMI/resources/Homer2) was then used to project these points onto an each participant's head atlas using a relaxation algorithm. A single subject's projected probe geometry is shown in Figure 2b. The projected geometry was used to run Monte Carlo simulations (with 100 million photons) based upon a GPU-dependent Monte Carlo algorithm (Fang and Boas, 2009). The output of the Monte Carlo simulations yield a sensitivity distribution that is representative of the sensitivity of each channel to detecting changes in the cortical absorption of near infrared light. Thus, we obtained sensitivity profiles for each of the 28 channels for each participant.

The sensitivity profiles and the head volumes were converted to nifti images. Subject-specific head volumes were skull-stripped and transformed from the *AtlasViewer*GUI space to the native subject space using an affine transform (*BRAINSFit in Slicer 3D*). This transformation matrix was also applied to the sensitivity profiles to move them back to the native subject space (*BRAINSResample in Slicer3D*). The sensitivity profiles for each participant were summed together to create a subject-specific mask that represented the spatial distribution of cortical volume that fNIRS signals were most likely recorded from.

These subject-specific masks were thresholded to include voxels with an optical density of greater than 0.0001, a robust threshold value that is derived from our previous work (Wijeakumar et al., 2015).

Next, the head volumes in native subject space were transformed from native subject space to MNI space using an affine transform with nine parameters (using *3dAllineate*). These transformation matrices were further used to transform the subject-specific masks to MNI space. These subject-specific masks were summed together and masked such that only voxels that contained a value greater than 7 were retained. Thus, we created a group intersection mask across participants wherein at least seven out of thirteen participants contributed to a voxel. A decimated and smoothed version of a single participant's head volume and the group intersection mask (created using *ModelMaker in Slicer 3D*) is shown in Figure 2c.

2.6. Image Reconstruction (Step 8-9 in Figure 3)

The majority of fNIRS studies have utilized channel-based time-domain analyses. Although informative, such approaches provide only limited information about localization, typically with reference to the 10-20 positions of channels on the head. This can be problematic, because the positions of sources and detectors invariably differ across participants, particularly when working with special populations such as infants, young children, or clinical populations who have difficulty sitting still. Moreover, channel-based analyses fail to capitalize on the fact that nearby fNIRS channels often record overlapping signals; such information is lost by treating each channel as independent. Finally, the absence of good localization tools in fNIRS research limits comparisons with the large body of fMRI research. Hence, the goal of our study was to validate a new image reconstruction approach in a cognitive task.

To generate functional images from the fNIRS data, the beta coefficients obtained for each condition, channel, and participant (see section 2.4) must be combined with the sensitivity profiles obtained from the Monte Carlo simulations (see section 2.5) to create voxel-based changes in HbO and HbR concentration.

The relationship between the hemodynamic response (estimated by the beta coefficients from the GLM) in HbO/HbR concentration and that in delta-optical density is given by:

$$\beta_{dOD}^{\lambda} = ppf^{\lambda} \,.\, d \,.\, \varepsilon_{HbO}^{\lambda} \,.\, \beta_{HbO} + \; ppf^{\lambda} \,.\, d \,.\, \varepsilon_{HbR}^{\lambda} \,.\, \beta_{HbR} \qquad (1)$$

where, *d* is the source-detector distance, ε is the extinction coefficient for each wavelength (λ) and *ppf* is the partial pathlength factor (Li et al., 2004).

Equation (1) can be re-written to accommodate the forward model and betas from each channel for each wavelength to estimate voxel-wise changes in HbO and HbR concentrations,

$$\begin{bmatrix} d \,.\, \varepsilon_{HbO}^{\lambda 1} \,.\, \beta_{HbO} + \; d \,.\, \varepsilon_{HbR}^{\lambda 1} \,.\, \beta_{HbR} \\ d \,.\, \varepsilon_{HbO}^{\lambda 2} \,.\, \beta_{HbO} + \; d \,.\, \varepsilon_{HbR}^{\lambda 2} \,.\, \beta_{HbR} \end{bmatrix} = \begin{bmatrix} \varepsilon_{HbO}^{\lambda 1} \,.\, F^{\lambda 1} & \varepsilon_{HbR}^{\lambda 1} \,.\, F^{\lambda 1} \\ \varepsilon_{HbO}^{\lambda 2} \,.\, F^{\lambda 2} & \varepsilon_{HbR}^{\lambda 2} \,.\, F^{\lambda 2} \end{bmatrix} . \begin{bmatrix} \Delta HbO_{vox} \\ \Delta HbR_{vox} \end{bmatrix} \qquad (2)$$

where, *F* is the channel-wise sensitivity volumes from the Monte Carlo simulations. ΔHbO_{vox} and ΔHbR_{vox} are voxel-wise relative changes in HbO and HbR concentrations – this is what we want to estimate in the image reconstruction process. *Note that* **β** *and* **F** *are obtained for each channel and are represented as arrays within the matrix above.*

We can re-write equation Equation (2) as,

$$Y = L \,.\, X \qquad (3)$$

where,

$$Y = \begin{bmatrix} \beta_{dOD}^{\lambda 1} \\ \beta_{dOD}^{\lambda 2} \end{bmatrix}$$

$$L = \begin{bmatrix} \varepsilon_{HbO}^{\lambda 1} \,.\, F^{\lambda 1} & \varepsilon_{HbR}^{\lambda 1} \,.\, F^{\lambda 1} \\ \varepsilon_{HbR}^{\lambda 2} \,.\, F^{\lambda 2} & \varepsilon_{HbR}^{\lambda 2} \,.\, F^{\lambda 2} \end{bmatrix}$$

$$X = \begin{bmatrix} \Delta HbO_{vox} \\ \Delta HbR_{vox} \end{bmatrix}$$

Inverting *L* to solve for *X* results in an ill-conditioned and under-determined solution that might be subject to rounding errors. An alternative is to use a popular regularization method called Tikhonov regularization (Tikhonov A., 1963). In this case, the above 'system' can be replaced by a regularized 'system'. The solution is given by the Gauss-Markov equation,

$$X = (L^T L + \; \lambda . I)^{-1} \, L^T \,.\, Y \qquad (4)$$

where λ is a regularization parameter that determines the amount of regularization and I is the identity operator.

The solution to (4) can be found by minimizing the cost function (Calvetti et al., 2000),

$$cost \min X = |L.X - Y|^2 + \lambda . |X - X_o|^2 \quad (5)$$

where the size of the regularized solution is measured by the norm $\lambda . |X - X_0|^2$. X_0 is a priori estimate of X, which is set to zero when no priori information is available. Picking the appropriate regularization parameter is dependent on the trade-off between fitting Y and maintaining a small residual (if too much regularization is applied) and eliminating the contributions of data and rounding errors (if too little regularization is applied). Hence, an L-curve is plotted between the norms of the solution and the residual. The corner of this L-curve is identified and the corresponding regularization parameter is used to estimate X.

Here X is determined for each chromophore and condition (12 conditions) separately. Once we solve (5), we have a voxel-wise estimate of the concentration data. Thus, we have moved from our best estimate of the channel-wise concentration data for each condition (from the GLM) and combined this information with the sensitivity profiles to create an estimate of the voxel-wise relative changes in concentration for each condition, for each subject and, for each chromophore. These maps were transformed to the MNI space by using the transformation matrix (affine transformation with 9 parameters) generated from transforming the subject-specific head volumes. Finally, these voxel-wise relative changes in chromophore concentration were multiplied by the group intersection mask and moved forward to the group analyses.

2.7. fMRI Acquisition and Processing (Steps 10-12 in Figure 3)

fMRI data were collected in a 3T Siemens TIM Trio scanner using a 12-channel head coil. Anatomical T1 weighted volumes were collected using an MP-RAGE sequence. Functional BOLD imaging was acquired using an axial 2D echo-planar gradient echo sequence with the following parameters: TE=30ms,

TR=2000ms, flip angle=70°, FOV=240x240mm, matrix=64x64, slice thickness/gap=4.0/1.0mm, and bandwidth=1920Hz/pixel.

AFNI was used to perform standard pre-processing such as slice timing correction, outlier removal, motion correction, and spatial smoothing (Gaussian FWHM=5mm). Nuisance regressors of motion correction, baseline drift, and 12 standard model regressors (12 conditions – as specified in section 2.4) were used in a general linear model (using *3dDeconvolve*). Polynomials of the third order were used as regressors to account for drift in the data and serve as a high pass filter. *Note that, BOLD data were analyzed using conventional parameters from fMRI literature and not with parameters used for the fNIRS analyses.* The onset of the sample array for each condition was convolved with a canonical single parameter gamma variate function. This function was identical to that used in the GLM for the fNIRS data. Betamaps (in percent BOLD signal) were obtained for each model regressor and for each participant. An affine transformation was applied to each individual's skull-stripped T1 scan to transform it to the MNI space. This transformation matrix was used to transform the betamaps to the MNI space. Finally, these betamaps were multiplied by the group intersection mask (see step 8) and moved forward to the group analyses.

2.7. Statistical Analysis

2.7.1 Behavioral Analysis

Only correct trials across Load (2, 4 and 6) and Trial type (Same and Different) were analyzed using a two-factorial ANOVA in SPSS 21.

2.7.2 Correlations between BOLD and NIRS signals within the VWM network (Step 13 in Figure 3)

Previous validation studies have reported good spatial and temporal correlations when comparing fNIRS and fMRI signals. In the current study, we wanted to investigate whether the betamaps produced from our image reconstruction methods were spatially correlated with the BOLD betamaps.

We carried out Pearson's voxel-wise correlations between the BOLD betamaps and relative changes in HbO and HbR concentration for each of the 12 conditions separately. We thresholded each of our correlation maps using a voxel-wise threshold of $p<0.05$, $\alpha<0.05$ and a cluster size of 28 voxels (obtained using *3dClustSim*) based on the size of the group intersection mask, size of the 3D grid of the image (91 x 109 x 91 vioxels), and the voxel size (2mm) of the image. Further, voxels were clustered together only if faces or edges touched. For specific exemplar clusters, average R-values were calculated within each cluster for each participant using *3dROIstats*.

To estimate the depth of the voxel with the highest correlation in each cluster, the shortest Euclidean distance between the voxel with the highest correlation and the surface of the brain was calculated.

2.7.3 Multi-factorial effects common to BOLD and NIRS (Step 14 in Figure 3)

Previous research with fMRI has reported key regions in the frontal, parietal, and temporal cortices involved in processing changes in a working memory task. Hence, in the current study, we examined whether the same regions showing an effect in working memory processing, for instance, with fMRI would also show comparable parametric effects with fNIRS.

To achieve this, the BOLD betamaps were analyzed at the group level using a three-factor ANOVA with Load (2,4,6), Trial type (Same, Different), and Accuracy (Correct, Incorrect) as within-subjects factors. Similarly, for fNIRS, the betamaps for the relative changes in HbO and HbR concentration were analyzed at the group-level using two separate 3-factor ANOVAs (Load x Trial type x Accuracy), one for each chromophore. The main effects and interactions from all three ANOVAs (BOLD, HbO and HbR) were thresholded to correct for familywise errors (voxel-wise threshold of $p<0.05$, $\alpha<0.05$, and a cluster size of 28 voxels). We then identified significant clusters where both fMRI and fNIRS showed the same statistically significant main effect or interaction. Further, the spatial maps

for the main effect of Load were compared between BOLD and fNIRS to highlight exemplary effects.

3. Results

3.1. Behavioral results

Figure 4 shows the accuracy rates in percentage across Load and Trial types. Briefly, there were main effects of load ($F_{(2,24)}$=57.40, p<0.001) and Trial type ($F_{(1,12)}$=50.85, p<0.001) and the interaction between Load and Trial type ($F_{(2,24)}$=57.40, p<0.001) was also significant. Post-hoc comparisons revealed that same trials had higher accuracy rates than different trials (p<0.001). Accuracy rates decreased with an increase in Load (p<0.05). Further comparisons of the interaction between Trial type and Load revealed that accuracy significantly decreased as a function of Load only for the different trials (p<0.005). Further, only at Load 4 and 6, did same trials have significantly higher accuracy rates than different trials (p<0.001).

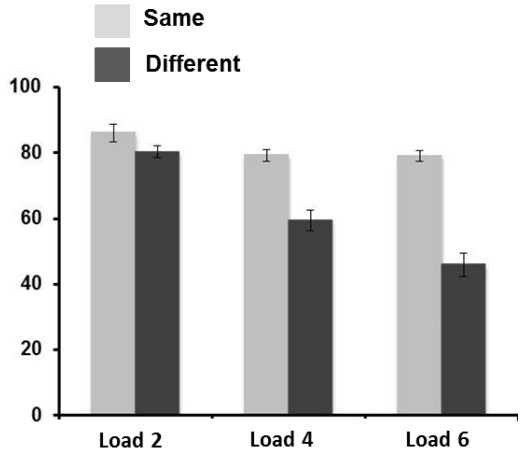

Figure 4. Accuracy (%) plotted across same and different trials for Loads 2,4 and 6.

3.2 Correlations between BOLD and image-reconstructed fNIRS signals

Figure 5 shows a montage of the cortical regions where there was a significant correlation between BOLD and HbO/HbR concentration following familywise correction. As can be seen in the figure, the two signals correlated significantly across many areas central to the VWM network, including middle (MFG), inferior (IFG) and superior frontal gyrus (SFG), superior (SPL) and

inferior parietal lobule (IPL), superior (STG) and middle temporal gyri (MTG), precuneus and cuneus. *Note that regions of overlap across HbO-BOLD and HbR-BOLD correlations do not necessarily occur across the same conditions.*

When we examined the nature of these correlations in detail, we observed significant positive and negative correlations between HbO and BOLD and HbR and BOLD signals. Positive HbO-BOLD and positive HbR-BOLD correlations accounted for 22.9% and 29.7% of the all the correlations, respectively. Interestingly, negative HbO-BOLD and negative HbR-BOLD correlations accounted for 25.6 % and 21.6 % of all the correlations, respectively. *Note that a voxel could show positive correlations between HbO and BOLD for a specific condition and negative correlations for another condition.* A complete breakdown of the correlation types across conditions is reported in Supplemental table T1.

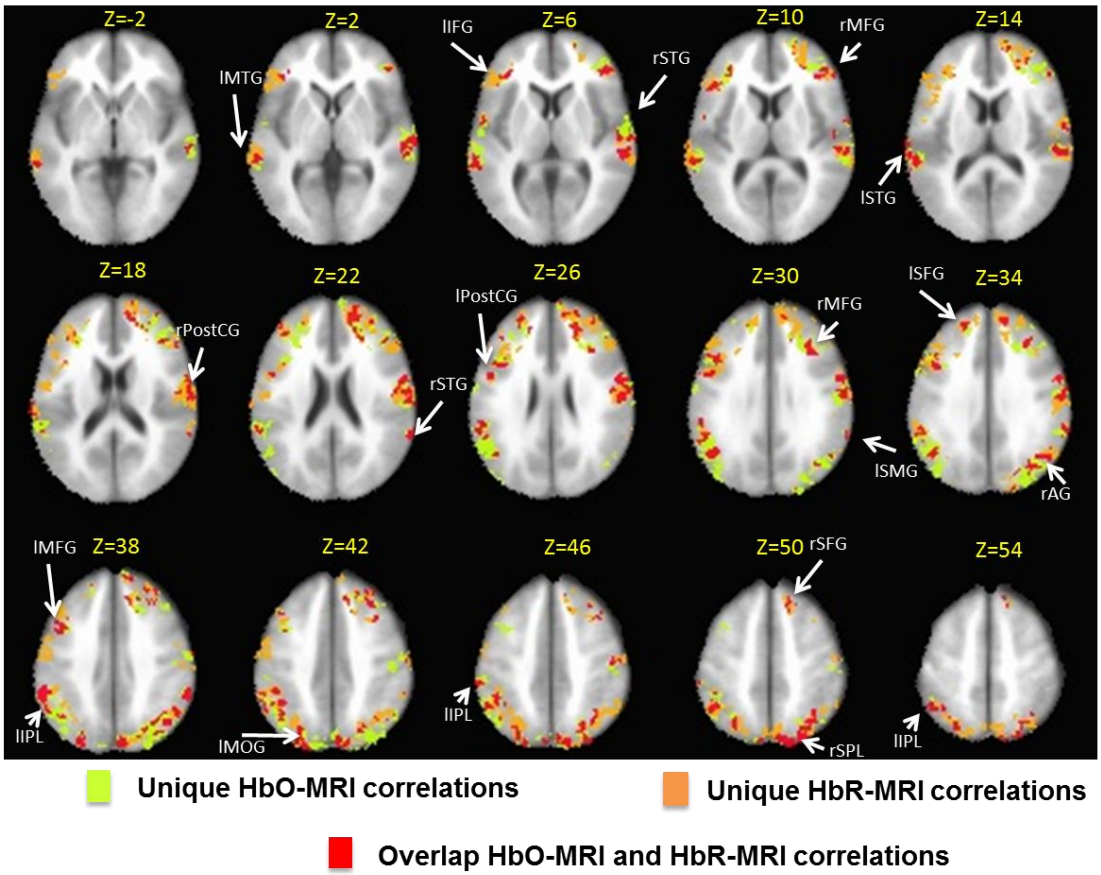

Figure 5. Montage showing correlations between relative changes in HbO/HbR concentration and percent BOLD signal change. Note that the spatial distributions have been masked to create

binary images. The green color indicates clusters with significant HbO-MRI correlations, but not HbR-MRI correlations; orange indicates clusters with significant HbR-MRI correlations, but not HbO-MRI correlations; red indicates clusters with significant correlations between both chromophores and MRI.

When pooled across loads, Hit and CR conditions showed more significant correlations between HbO and fMRI (Hits = 1824 voxels and CR = 1243 voxels) than the FA and Miss conditions (see Supplementary Table T1 for details). Further, we were particularly interested in the Load 4 condition as previous research has suggested that the capacity limit for visual working memory is around four items (Luck and Vogel, 1997). Thus, to examine the nature of the correlations in greater detail, we focused on the Hit4 and CR4 conditions.

Figures 6 and 7 show positive correlations across voxels for HbO-BOLD and HbR-BOLD correlations for the Hit4 and CR4 conditions, respectively. These figures also show scatter plots of correlation values averaged across voxels in clusters that met the family-wise correction threshold (28 voxels). For the Hit4 condition, the magnitude of the peak correlation values from each significant cluster for positive HbO-BOLD and positive HbR-BOLD correlations ranged from 0.71 to 0.99. For the CR4 condition, the peak correlation values from each significant cluster for positive HbO-BOLD and positive HbR-BOLD correlations ranged from 0.62 to 0.97. As is evident from the figures, there were clusters with significant positive HbO-BOLD correlations in the rSPL for both Hit4 and CR4 conditions. Similarly, there were clusters with significant positive HbR-BOLD correlations in the rIFG for both Hit4 and CR4 conditions (for a complete listing of clusters with significant correlations, see supplementary tables T2-T5).

Previous studies have reported that the depth of voxels showing correlations between BOLD and fNIRS measures were between 15-20 mm (Cui et al., 2011; Schroeter et al., 2006). Thus, we estimated the depth of the voxels within each cluster with the highest correlations between HbO and BOLD and HbR and BOLD for Hit4 and CR4 conditions. The mean depth (from the surface of the brain) of the most highly correlated voxels between fNIRS and BOLD was 5.6±0.8mm (positive HbO-BOLD correlation depth = 4 mm and positive HbR-

BOLD correlation depth = 7.1 mm). Taken together with an average estimation for scalp and skull thicknesses (11-13 mm), the depth of these correlations from the surface of the scalp is between 15-20 mm, which is in agreement with these previous studies (Cui et al., 2011; Schroeter et al., 2006).

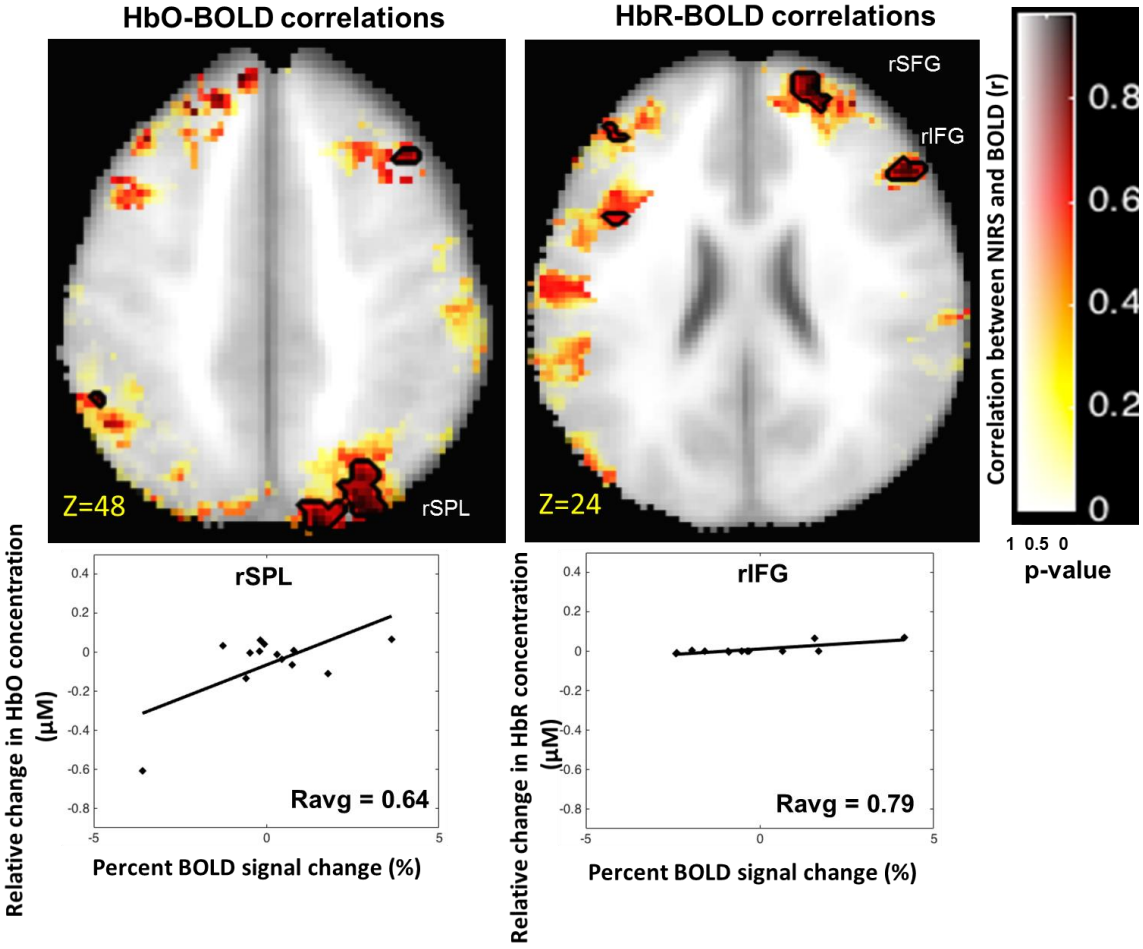

Figure 6. Positive HbO-BOLD and HbR-BOLD correlations for the Hit4 condition. Clusters that reached significance ($p<0.05$) are shown within contours. Transparency of clusters in the image indicates significance (as represented by the x-axis of the color scale). Scatter plots for selected clusters are shown below the respective correlation image. Ravg (shown in the correlation plots) was obtained for each participant (N=13) by averaging the r values across all voxels of a significant cluster.

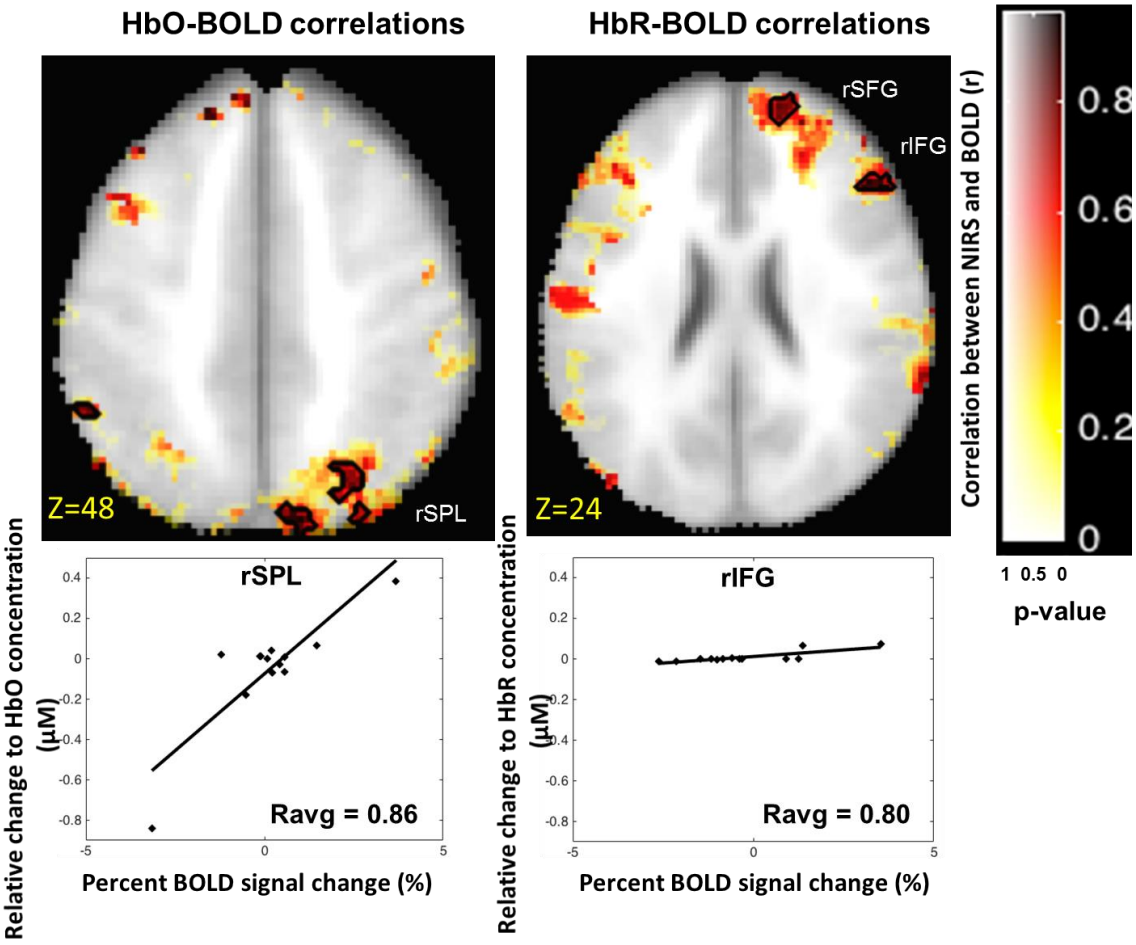

Figure 7. Positive HbO-BOLD and HbR-BOLD correlations for the CR4 condition. Clusters that reached significance ($p<0.05$) are shown within contours. Transparency of clusters in the image indicates significance (as represented by the x-axis of the color scale). Scatter plots for selected clusters have been shown below the respective correlation image. Ravg (shown in the correlation plots) represents correlation of data from 13 participants obtained from averaging r values across all voxels of a significant cluster.

3.4 Overlapping multi-factorial VWM effects

The current validation study is embedded within a cognitive task with parametric manipulations. Do fNIRS and fMRI detect the same changes in activation levels as a function of these parametric manipulations? To evaluate this question, we conducted three 3-factor ANOVAs -- one for BOLD, one for HbO, and one for HbR (see Methods)--and examined the degree to which significant effects overlapped and yielded the same activation patterns across experimental manipulations.

Figure 8 shows a montage image of the overlapping and unique effects from the significant ANOVA results following family-wise correction. There is overlap between the fNIRS and BOLD effects across parts of the fronto-parieto-temporal regions such as IPL, MFG, SFG and IFG. Although there is overlap between the modalities, however, the fNIRS effects are much more focal compared to the spatial distribution of the BOLD effects. As we discuss below, this may reflect differences in the signal-to-noise ratio of the two modalities. *Note that overlap between HbO, HbR and MRI accounted for only 15 voxels (summed across all cortical regions) and this has not been shown in Figure 8.*

Within the regions of overlap, a central issue is whether the two modalities are detecting the same parametric effect. Tables 1 and 2 show all clusters that had overlapping main effects and interaction effects for HbO and BOLD and HbR and BOLD ANOVAs, respectively. There was substantial overlap in effects across key parts of the visual working memory network. This included large clusters with overlapping Load main effects in rIPL and rMFG for the comparison between HbO and BOLD. There were also large clusters with overlapping Load x Trial x Accuracy effects in lSFG and lIFG, as well as a large cluster with an overlapping Accuracy main effect in rIFG.

Figure 9 shows the activation pattern in two rIPL clusters for illustration showing an increase in HbO and BOLD as the working memory load increased from 2 to 6 items ($p<0.05$).

For the comparison between HbR and BOLD, we found large clusters with overlapping Load main effects in right superior occipital gyrus (rSOG) and right

postcentral gyrus. There was also a large cluster with an overlapping Load x Trial x Accuracy interaction in the left angular gyrus (AG), and a large cluster with an overlapping Accuracy main effect in lIFG. In Figure 10, we observed an increase in BOLD and a decrease in HbR activation in the rSOG cluster (Load Main effect) as the working memory load increased from 2 to 6 showing ($p<0.05$). Albeit, in different cortical areas, HbR activation in rSOG shows an opposite trend to that of HbO and BOLD activation in rIPL.

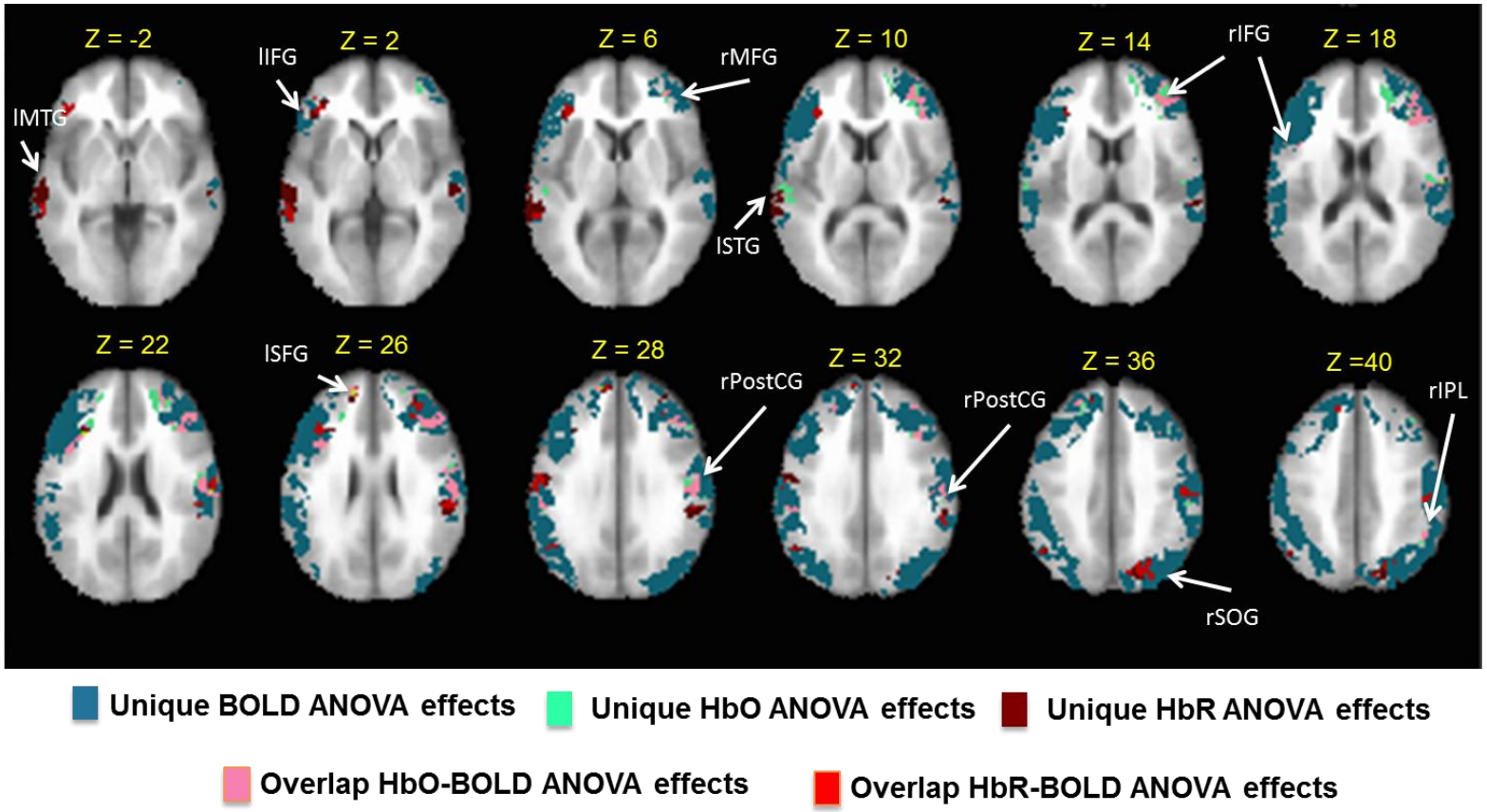

Figure 8. Montage showing overlap between ANOVA effects from HbO and HbR concentration and percent BOLD signal change. Note that the spatial distributions have been masked to create binary images. The teal color indicates clusters with significant unique BOLD ANOVA effects; green color indicates clusters with significant unique HbO ANOVA effects; brown color indicates clusters with significant unique HbR ANOVA effects; pink color indicates clusters with significant overlap between HbO and BOLD ANOVA effects and red color indicates clusters with significant HbR-BOLD ANOVA effects. *Note that overlap between HbO, HbR and MRI accounted for only 15 voxels (summed across all cortical regions) and not shown in Figure 8.*

588 Table 1. Regions commonly activated by the main effects and interaction effects of Load,
589 Accuracy and Trial for HbO and BOLD ANOVAs. *Note that, there were no common regions of*
590 *overlap for the Trial main effect and the Accuracy X Trial interaction.*

Region	Hemi	Center of Mass MNI Coordinates (LPI orientation)			Size (mm^3)
		x	y	z	
Load Main effect					
Inferior parietal lobule	R	50.8	-50.2	42.9	160
Inferior parietal lobule	R	50.3	-57	46.3	144
Middle frontal gyrus	R	37.1	45.9	11.6	824
Middle frontal gyrus	R	39.1	21.8	34.8	232
Middle frontal gyrus	R	38.5	56	12.5	64
Middle frontal gyrus	R	39.6	29.2	40	40
Middle frontal gyrus	R	38	57	0	16
Middle frontal gyrus	R	36	56	2	8
Middle frontal gyrus	R	42	46	20	8
Middle frontal gyrus	R	38	24	40	8
Load x Accuracy					
Superior frontal gyrus	L	-22.3	40.6	33.7	56
Superior frontal gyrus	L	-24.7	44.7	38	24
Superior frontal gyrus	L	-21.3	45.3	40	24
Superior frontal gyrus	L	-18	44	36	8
Load x Trial					
Postcentral gyrus	R	52	-5.8	27.8	80
Load x Trial x Accuracy					
Superior frontal gyrus	L	-14.9	54.3	27.4	224
Inferior frontal gyrus	L	-38.9	13.5	24.6	176
Inferior frontal gyrus	R	46	30	26	8
Inferior frontal gyrus	R	44	28	28	8
Accuracy Main effect					
Middle frontal gyrus	R	44	41	20	16
Middle frontal gyrus	R	44	32	22	8
Inferior frontal gyrus	R	46.7	30.4	19	448
Inferior frontal gyrus	R	42	29	24	16
Inferior frontal gyrus	R	40	32	14	8
Inferior frontal gyrus	R	44	36	16	8
Inferior frontal gyrus	R	40	26	24	8
Postcentral gyrus	R	54	-3	24	16

591

Table 2. Regions commonly activated by the main effects and interaction effects of Load, Accuracy and Trial for HbR and BOLD ANOVAs. *Note that, there were no common regions of overlap for Trial main effect and Accuracy x Trial interaction.*

Region	Hemi	Center of Mass MNI Coordinates (LPI orientation)			Size (mm^3)
		x	y	z	
Load Main effect					
Superior occipital gyrus	R	25.7	-75	38.5	568
Superior occipital gyrus	R	22	-78	42	8
Postcentral gyrus	R	54.4	-20.3	39.1	552
Load x Accuracy					
Superior temporal gyrus	R	63	-30	10	16
Load x Trial					
Inferior frontal gyrus	L	-52	36	4	8
Load x Trial x Accuracy					
Angular gyrus	L	-51.8	-60.4	35.1	88
Angular gyrus	L	-47	-58	30	16
Angular gyrus	L	-48	-60	32	8
Middle temporal gyrus	L	-61.2	-34.8	3.6	40
Middle temporal gyrus	L	-62	-30	2	8
Middle temporal gyrus	L	-64	-30	4	8
Accuracy Main effect					
Inferior frontal gyrus	L	-39.2	25.4	26.7	152
Supramarginal gyrus	R	58	-40	34	40
Middle temporal gyrus	L	-64	-42	8	24
Middle temporal gyrus	L	-60	-40	7	16
Middle temporal gyrus	L	-62	-40	4	8
Superior temporal gyrus	R	60	-16	0	8

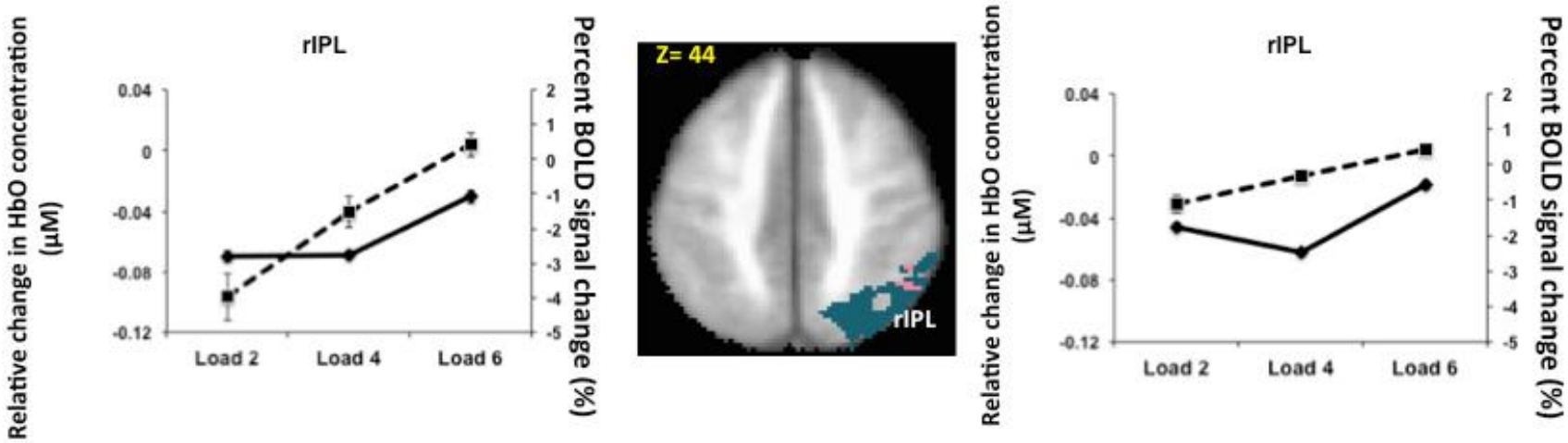

Figure 9. Main effect of Load in two rIPL clusters. Bold lines indicate BOLD activation and dashed lines indicate HbO activation.

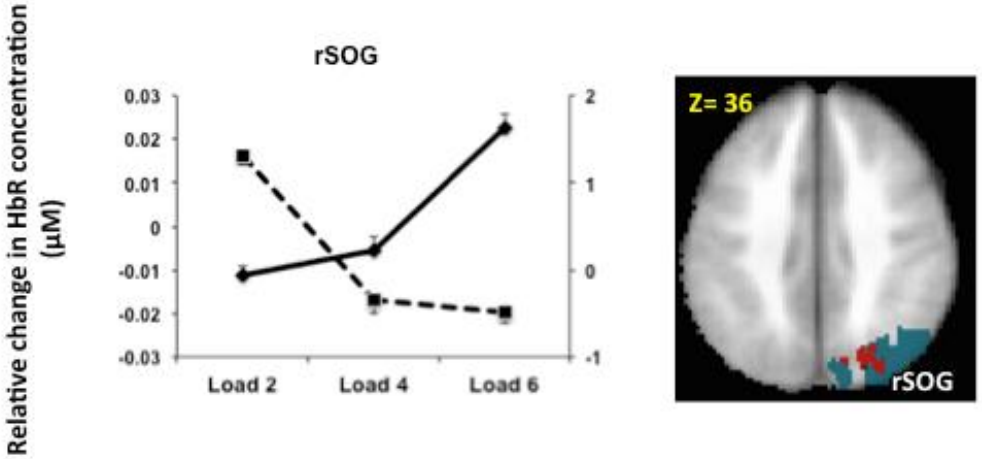

Figure 10. Main effect of Load in a rSOG cluster. Bold lines indicate BOLD activation and dashed lines indicate HbR activation.

4. Discussion

The objective of the current study was to validate a novel methodological pipeline to move fNIRS analyses from conventional channel-based analyses on the surface of the head to voxel-based analyses within the brain volume. There are several advantages of the image reconstruction approach. First, this approach aligns the fNIRS data across participants, factoring in differences in optode placement due to experimenter errors and/or movement of the participant. The latter is likely to be a key source of variation when dealing with infants, young children, and clinical populations who have difficulty sitting still. Second, the image reconstruction approach can capitalize on cases where nearby fNIRS channels record from overlapping cortical areas, potentially boosting the strength of effects that are weak and distributed across channels. Third, the image reconstruction approach allows for direct comparisons with fMRI data. Finally, this approach facilitates analysis in that fMRI analysis tools can be readily used with fNIRS data. This makes it easy to port advanced analysis techniques from the fMRI literature to the fNIRS literature.

These advantages of the image reconstruction approach are evident in Figure 11. In this figure, we show surface projections of the sensitivity volumes for a single fNIRS channel across the 13 participants. The single channel's positions across the 13 participants have been shown using the four 3D images (top left image shows this channel placement on 4 participants and top right, bottom left and right show this channel placement on 3 participants each). This particular channel showed considerable variation in position on the head surface. The image reflects the challenge of placing fNIRS optodes on the head relative to the 10-20 system. Variation was likely introduced when we positioned participants inside the scanner bore causing optodes to shift slightly as participants laid down. Consequently, this channel was recording from different parts of cortex across participants.

In stark contrast to this variable cloud on the brain surface, the image at the center shows results within the brain volume underneath the region where this fNIRS channel was placed. The cluster shows a significant main effect of

Load in the rIPL (obtained from Figure 9 – HbO-BOLD effect) from the image reconstruction approach. The fNIRS cluster precisely overlaps with a localized main effect of Load from the fMRI analysis. The fNIRS analysis was also straightforward to conduct using an fMRI analyses toolbox such as AFNI.

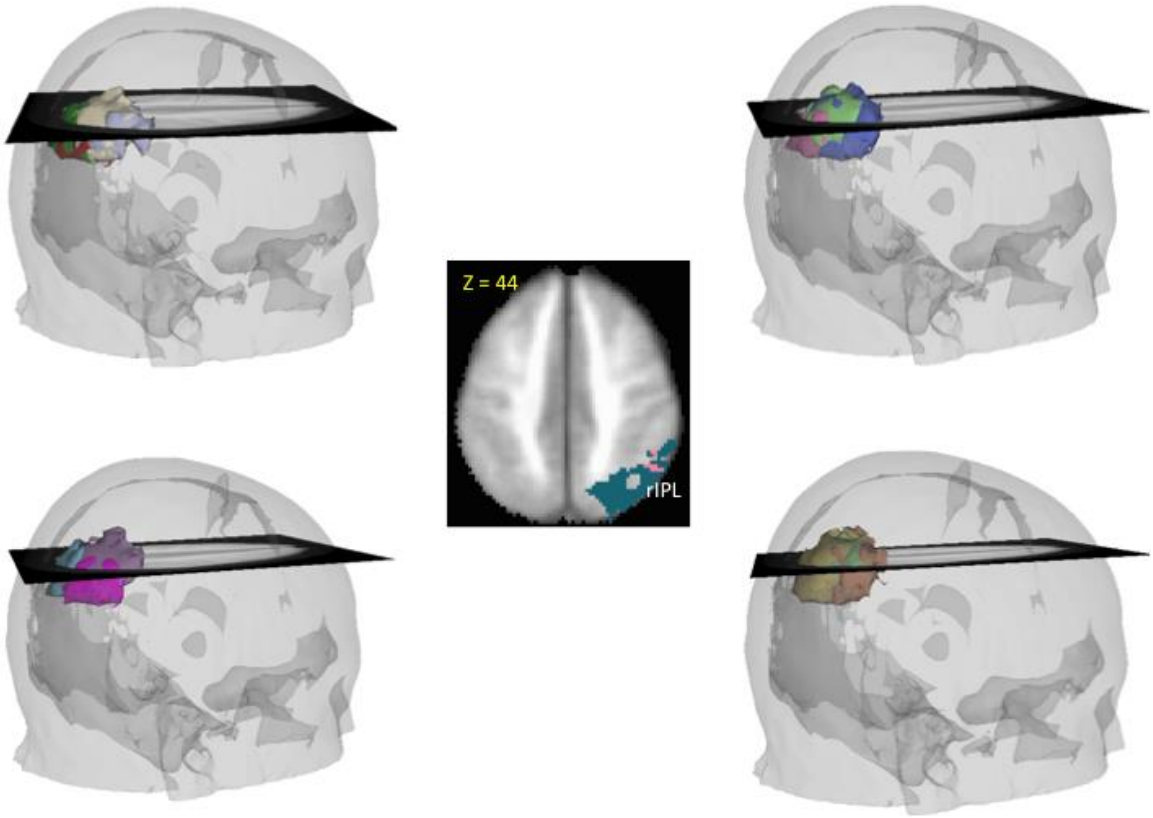

Figure 11. Variations of a channel across 13 subjects (shown in multiple colors across the different 3D images). Image at the center shows an axial slice for the Load effect (obtained from Figure 9 – HbO-BOLD effects) in rIPL.

In the sections that follow, we elaborate on our validation findings. We focus first on the correlational results. Next, we evaluate the multi-factorial effects, highlighting results showing the parametric manipulation of the memory load.

4.1. Correlations between fNIRS and fMRI

Previous concurrent fNIRS and fMRI studies have established that results from both modalities are well-correlated across sensory tasks (Cui et al., 2011; Gagnon et al., 2012; Huppert et al., 2006, 2005; Sassaroli et al., 2005; Sato et

al., 2013; Schroeter et al., 2006; Strangman et al., 2002; Wijeakumar et al., 2012a). However, there is less work that has examined the correspondence between both techniques in cognitive tasks (for exceptions, see Cui et al., 2011; Sato et al., 2013).

In the current study, fNIRS measures were correlated with BOLD measures in a number of cortical regions that spanned the frontal, parietal, temporal, and occipital cortices. There were both positive and negative correlations between HbO and HbR and BOLD signals. Collectively, positive HbR-BOLD correlations were more frequent than positive HbO-BOLD correlations. Interestingly, there is debate on the exact role of HbR during experimental tasks, an issue which is spurred on by studies showing strong correlations between HbR and BOLD (Huppert et al., 2006, 2005; Kleinschmidt et al., 1996; MacIntosh et al., 2003; Mehagnoul-Schipper et al., 2002; Murata and Sakatani, 2002; Sato et al., 2013; Siegel et al., 2003; Toronov et al., 2001). Other studies, by contrast, have shown higher correlations between HbO and BOLD (Cui et al., 2011; Heinzel et al., 2013; Hoshi and Tamura, 1993; Strangman et al., 2002; Yamamoto and Kato, 2002), and a few studies have reported significant correlations between total hemoglobin concentration and BOLD (e.g., Hess et al., 2000). These findings highlight the need for clarity on precisely how HbO, HbR, and BOLD are related.

There is also a need for clarity on what negative correlations between HbO and BOLD and HbR and BOLD represent. A few studies have reported that signals obtained from fNIRS are sensitive to microvasculature such as arterioles and venules instead of larger vasculature such as arteries and veins as the light is unlikely to be detected back at the scalp in the latter case (Boushel et al., 2001; Cannestra et al., 2001; Liu et al., 1995a, 1995b; Schroeter et al., 2006). In On the other hand, fMRI is likely to be more sensitive to bigger vessels. These anatomical differences taken within the context of a time and space-sensitive neural process like VWM, could explain the presence of negative correlations between modalities. Future validation studies that use cognitive tasks could

examine both spatial and temporal aspects of these signals to better understand the relationship between HbO, HbR, and BOLD.

How do previous reports of correlations between fNIRS and fMRI compare with those reported in the current study? Cui et al. (2011) projected a marker from each channel from the scalp to the brain and correlated an average as well as voxel-wise BOLD signals from a 5mm radius of the projected points with that specific channel's fNIRS signal (Cui et al., 2011). They showed good spatial correspondence between fMRI and fNIRS across the frontal and parietal cortices in response to an n-back visual working memory task. They found that the highest correlation between HbO and BOLD was 0.26 and the HbR and BOLD was 0.23. An earlier study by Okamoto and colleagues observed almost equal correlation values between HbO and BOLD and HbR and BOLD during an apple-peeling exercise (Okamoto et al., 2004). Further, they found that the highest correlations were observed in the middle frontal and inferior parietal areas. Overall, these results are in agreement with findings from the current study wherein the highest correlations were observed in SPL and IFG. That said, we observe much higher correlations between fNIRS and fMRI activation than shown in previous studies.

An interesting observation from the correlation scatterplots was that the variation in the fNIRS signal was greater for SPL than for IFG. The frontal cortex is responsible for the maintenance of goals and abstract representations of the task whereas parietal regions are responsible for feature-processing and visual stimulus encoding (D'Esposito and Postle, 2015). Given these functions, it is possible that increased variability in SPL might be a reflection of inter-individual differences in stimulus processing. Future work will need to explore the extent to which variations in brain activation might reflect inter-individual differences in performance.

In another study, Sato et al. used photon path distributions to weight averaged BOLD signals from grey matter voxels and correlated those with fNIRS signals in the channels that 'supervised' those voxels (Sato et al., 2013). They conducted correlations between time-domain signals and found that HbR was

711 marginally more correlated with BOLD than HbO. They reported that the middle
712 of prefrontal cortex, around the inferior parietal and superior temporal cortices
713 showed a high correlation between BOLD and fNIRS signals. In the current
714 study, we found that both positive HbO–BOLD and HbR-BOLD showed similar
715 ranges of correlations. Further, the number of correlated voxels for HbR-BOLD
716 was slightly higher than for HbO-BOLD.
717 Another interesting metric that has been reported in previous studies is the
718 depth at which these correlations have been observed. Schoreter et al. (2006)
719 found that the highest correlations between fNIRS and fMRI signals in response
720 to visual stimulation occurred between 15-20 mm from surface of the scalp
721 (Schroeter et al., 2006). Cui et al. (2011) observed that peak correlations were
722 observed at a depth of 4 voxels, which translated to approximately 16 mm [as per
723 the voxel size they specified] (Cui et al., 2011). In the current study, voxels with
724 the highest correlations within each cluster were observed at a mean depth of 8.8
725 mm of the *cortical surface*. Taken together with previously reported measures of
726 scalp and skull thickness estimates of about 11-13 mm (Oldendorf WH, 1969;
727 Strangman et al., 2014), our findings are in agreement with previous studies.
728 To summarize, both HbO and HbR were positively correlated with BOLD
729 in regions within the VWM network. These correlations were much higher in
730 magnitude but at a similar cortical depth as findings reported in previous studies.
731 This is an important finding given that there have been relatively few validation
732 studies using cognitive tasks and no previous validation studies using the image
733 reconstruction approach described in the present report. Although promising,
734 future work will be needed to more understand the nature of the correlations
735 (positive and negative) observed across neuroimaging modalities.
736
737 4.2. Multi-factorial effects of VWM
738 In addition to voxel-wise correlations across modalities, we examined
739 whether task-specific effects were also consistent in both the fNIRS and fMRI
740 data. To examine this question, we intersected effects from BOLD, HbO, and
741 HbR ANOVAs. We found overlapping effects across parts of the VWM network

as reported in previous fMRI studies (Linden et al., 2003; Luck and Vogel, 2013; Ma et al., 2014; Pessoa et al., 2002; Postle, 2015; Todd and Marois, 2004; Todd et al., 2005). These findings are also consistent with previous fNIRS studies that have investigated VWM, albeit using different analytical methods (Aoki et al., 2011; Cui et al., 2011; Cutini et al., 2011; McKendrick et al., 2014; Ogawa et al., 2014; Sato et al., 2013; Tsujimoto et al., 2004).

We found fNIRS and fMRI effects within regions of the frontal cortex that are important to VWM processing, including MFG. The MFG has been implicated in a number of VWM studies as a key site for the maintenance of rules, goals, and abstract representations that can guide other parts of the VWM network (Aoki et al., 2011; Barbey et al., 2013; Haxby et al., 2000; Munk et al., 2002; Pessoa and Ungerleider, 2004; Pessoa et al., 2002; Sala and Courtney, 2007; Sala et al., 2003; Sala-Llonch et al., 2012; Smith and Jonides, 1998).

Further, we also found robust fNIRS and fMRI activation in the IPL that increased with increasing working memory load. Our results are in agreement with Todd and Marois who showed that the activation in the inferior parietal sulcus increased with an increase in working memory load (Todd and Marois, 2004). Furthermore, Xu et al (2006) proposed that the inferior IPS is responsible for processing spatial information using a spatial indexing mechanism whereas LOC and superior IPS are important in processing object complexity (Xu and Chun, 2006). Similarly, Shahfritz et al (2006) showed that regions engaged in spatial attention were activated when objects were presented simultaneously as opposed to presented sequentially suggesting a link between spatial attention and feature binding (Shafritz and Gore, 2002). In our experiment, we only manipulated the color of the stimuli; however, it is plausible that the parietal activation we observed reflects a type of spatial indexing critical to feature binding.

Interestingly, the fNIRS ANOVA effects were focal in comparison to the effects from the BOLD ANOVA. We applied a liberal threshold of $p<0.05$ to our fMRI data relative to previous studies in an effort to maintain consistency across both approaches. However, it is possible that the fMRI signal requires a more

stringent threshold; much like that demonstrated in previous fMRI studies to show more focal effects. Clusters of activation after more stringent thresholding might be due to the fMRI technique, capturing certain aspects of the task that fNIRS could not. The current study is the first attempt at utilizing an ANOVA approach based on voxel-based fNIRS measures to compare activation with BOLD spatial distributions. We believe that more studies will need to be conducted to explore this novel finding.

Recent studies have discussed the importance of reporting both HbO and HbR effects to clarify what fNIRS signals can tell us about brain function (Tachtsidis and Scholkmann, 2016; Zhang et al., 2016). These studies also advocate removing systemic effects from cerebral and extra-cerebral signals, thereby leaving only task-relevant neural activation. For instance, Zhang et al. found that after removing global effects from the acquired signal, task-based HbO and HbR waveforms were more temporally and spatially consistent with each other. Indeed, this result was based on the assumption that true, task-related activation requires consistency between HbO and HbR signals. Critically, they applied their global signal correction on waveforms obtained from a block design of a finger-thumb tapping task. It will be important in future work to investigate whether these methods extend to event-related designs in cognitive tasks. In this context, we note that in the current study, we observed VWM effects amongst overlapping *and* non-overlapping regions of HbO, HbR and BOLD activation.

In addition to the removal of global systemic effects, it may be possible in the future to work to isolate HbO and HbR effects with a different experimental design. In the present study, we used relatively brief presentation times and short delays to mimic previous studies; however, longer delays might help isolate distinctive HbO and HbR patterns. For instance, several fMRI studies have explored neural activation patterns across the encoding, maintenance, and comparison phases by lengthening the duration of each phase (Linden et al., 2003; Todd & Marois, R., 2005). Such tasks might be useful in teasing apart the

complicated dynamics between cerebral blood flow, cerebral blood volume, and oxygen consumption.

In conclusion, findings from the present study successfully extend previous work, validating a novel methodological pipeline to move fNIRS analyses from the conventional channel-space to voxel-space within the volume of the brain. Results show fNIRS and fMRI are correlated across key VWM regions in the fronto-parietal network. Further, both modalities show spatial overlap in those clusters that are activated in response to parametric manipulations of the task including increasing working memory load. Most critically, we have demonstrated that the image-based fNIRS approach can effectively translate fNIRS signals into voxel space to enable direct comparison with fMRI results.

Acknowledgements

We would like to thank David A. Boas for his valuable input on this paper.

JPS acknowledges support from NSF BCS1029082.

References

Aoki, R., Sato, H., Katura, T., Utsugi, K., Koizumi, H., Matsuda, R., Maki, A., 2011. Relationship of negative mood with prefrontal cortex activity during working memory tasks: An optical topography study. Neurosci. Res. 70, 189–196. doi:10.1016/j.neures.2011.02.011

Barbey, A.K., Koenigs, M., Grafman, J., 2013. Dorsolateral prefrontal contributions to human working memory. Cortex 49, 1195–1205. doi:10.1016/j.cortex.2012.05.022

Boas, D. a., Elwell, C.E., Ferrari, M., Taga, G., 2014. Twenty years of functional near-infrared spectroscopy: Introduction for the special issue. Neuroimage 85, 1–5. doi:10.1016/j.neuroimage.2013.11.033

Bortfeld, H., Fava, E., Boas, D. a, 2009. Identifying cortical lateralization of speech processing in infants using near-infrared spectroscopy. Dev. Neuropsychol. 34, 52–65. doi:10.1080/87565640802564481

Bortfeld, H., Wruck, E., Boas, D. a., 2007. Assessing infants' cortical response to speech using near-infrared spectroscopy. Neuroimage 34, 407–15. doi:10.1016/j.neuroimage.2006.08.010

Boushel, R., Langberg, H., Olesen, J., Gonzales-Alonzo, J., Bülow, J., Kjaer, M., 2001. Monitoring tissue oxygen availability with near infrared spectroscopy (NIRS) in health and disease. Scand. J. Med. Sci. Sports 11, 213–222. doi:DOI 10.1034/j.1600-0838.2001.110404.x

Brigadoi, S., Cutini, S., Scarpa, F., Scatturin, P., Dell'Acqua, R., 2012. Exploring the role of primary and supplementary motor areas in simple motor tasks with fNIRS. Cogn. Process. 13, 97–101. doi:10.1007/s10339-012-0446-z

Brigadoi, S., Powell, S., Cooper, R.J., Dempsey, L.A., Arridge, S., Everdell, N., Hebden, J., Gibson, A.P., 2015. Evaluating real-time image reconstruction in diffuse optical tomography using physiologically realistic test data. Biomed. Opt. Express 6, 4719. doi:10.1364/BOE.6.004719

Calvetti, D., Morigi, S., Reichel, L., Sgallari, F., 2000. Tikhonov regularization and the L-curve for large discrete ill-posed problems. J. Comput. Appl. Math. 123, 423–446. doi:10.1016/S0377-0427(00)00414-3

853 Cannestra, a F., Pouratian, N., Bookheimer, S.Y., Martin, N. a, Beckerand, D.P.,
854 Toga, a W., 2001. Temporal spatial differences observed by functional MRI
855 and human intraoperative optical imaging. Cereb. Cortex 11, 773–82.
856 doi:10.1093/cercor/11.8.773
857 Cooper, R.J., Caffini, M., Dubb, J., Fang, Q., Custo, A., Tsuzuki, D., Fischl, B.,
858 Wells, W., Dan, I., Boas, D., 2012. Validating atlas-guided DOT: a
859 comparison of diffuse optical tomography informed by atlas and subject-
860 specific anatomies. Neuroimage 62, 1999–2006.
861 doi:10.1016/j.neuroimage.2012.05.031
862 Cui, X., Bray, S., Bryant, D.M., Glover, G.H., Reiss, A.L., 2011. A quantitative
863 comparison of NIRS and fMRI across multiple cognitive tasks. Neuroimage
864 54, 2808–2821. doi:10.1016/j.neuroimage.2010.10.069
865 Cutini, S., Scarpa, F., Scatturin, P., Jolicœur, P., Pluchino, P., Zorzi, M.,
866 Dell'Acqua, R., 2011. A hemodynamic correlate of lateralized visual short-
867 term memories. Neuropsychologia 49, 1611–21.
868 doi:10.1016/j.neuropsychologia.2010.12.009
869 D'Esposito, M., Postle, B.R., 2015. The Cognitive Neuroscience of Working
870 Memory. Annu. Rev. Psychol. 66, 186–219.
871 doi:10.1093/acprof:oso/9780198570394.001.0001
872 Druzgal, T.J., D'Esposito, M., 2003. Dissecting contributions of prefrontal cortex
873 and fusiform face area to face working memory. J. Cogn. Neurosci. 15, 771–
874 784. doi:10.1162/089892903322370708
875 Emir, U.E., Ozturk, C., Akin, a, 2008. Multimodal investigation of fMRI and fNIRS
876 derived breath hold BOLD signals with an expanded balloon model. Physiol.
877 Meas. 29, 49–63. doi:10.1088/0967-3334/29/1/004
878 Erdoğan, S.B., Yücel, M.A., Akın, A., 2014. Analysis of task-evoked systemic
879 interference in fNIRS measurements: Insights from fMRI. Neuroimage 87,
880 490–504. doi:10.1016/j.neuroimage.2013.10.024
881 Fabiani, M., Gordon, B.A., Maclin, E.L., Pearson, M.A., Brumback-Peltz, C.R.,
882 Low, K.A., McAuley, E., Sutton, B.P., Kramer, A.F., Gratton, G., 2014.
883 Neurovascular coupling in normal aging: A combined optical, ERP and fMRI

884 study. Neuroimage 85, 592–607. doi:10.1016/j.neuroimage.2013.04.113
885 Fang, Q., Boas, D. a, 2009. Monte Carlo simulation of photon migration in 3D
886 turbid media accelerated by graphics processing units. Opt. Express 17,
887 20178–20190. doi:10.1364/OE.17.020178
888 Ferrari, M., Quaresima, V., 2012. A brief review on the history of human
889 functional near-infrared spectroscopy (fNIRS) development and fields of
890 application. Neuroimage 63, 921–935.
891 doi:10.1016/j.neuroimage.2012.03.049
892 Fishburn, F.A., Norr, M.E., Medvedev, A. V., Vaidya, C.J., 2014. Sensitivity of
893 fNIRS to cognitive state and load. Front. Hum. Neurosci. 8, 1–11.
894 doi:10.3389/fnhum.2014.00076
895 Gagnon, L., Yücel, M. a., Dehaes, M., Cooper, R.J., Perdue, K.L., Selb, J.,
896 Huppert, T.J., Hoge, R.D., Boas, D. a., 2012. Quantification of the cortical
897 contribution to the NIRS signal over the motor cortex using concurrent NIRS-
898 fMRI measurements. Neuroimage 59, 3933–3940.
899 doi:10.1016/j.neuroimage.2011.10.054
900 Haxby, J. V, Petit, L., Ungerleider, L.G., Courtney, S.M., 2000. Distinguishing the
901 functional roles of multiple regions in distributed neural systems for visual
902 working memory. Neuroimage 11, 380–91. doi:10.1006/nimg.2000.0592
903 Heinzel, S., Haeussinger, F.B., Hahn, T., Ehlis, A.-C., Plichta, M.M., Fallgatter,
904 A.J., 2013. Variability of (functional) hemodynamics as measured with
905 simultaneous fNIRS and fMRI during intertemporal choice. Neuroimage 71,
906 125–134. doi:10.1016/j.neuroimage.2012.12.074
907 Hess, a, Stiller, D., Kaulisch, T., Heil, P., Scheich, H., 2000. New insights into
908 the hemodynamic blood oxygenation level-dependent response through
909 combination of functional magnetic resonance imaging and optical recording
910 in gerbil barrel cortex. J. Neurosci. 20, 3328–38.
911 Hoshi, Y., Tamura, M., 1993. Dynamic multichannel near-infrared optical imaging
912 of human brain activity. J Appl.Physiol 75, 1842–1846.
913 Huppert, T.J., Hoge, R.D., Diamond, S.G., Franceschini, M.A., Boas, D.A., 2006.
914 A temporal comparison of BOLD, ASL, and NIRS hemodynamic responses

915 to motor stimuli in adult humans. Neuroimage 29, 368–82.
916 doi:10.1016/j.neuroimage.2005.08.065
917 Huppert, T.J., Hoge, R.D., Franceschini, M.A., Boas, D.A., 2005. <title>A
918 spatial-temporal comparison of fMRI and NIRS hemodynamic responses to
919 motor stimuli in adult humans</title> 5693, 191–202.
920 doi:10.1117/12.612143
921 Kleinschmidt, a, Obrig, H., Requardt, M., Merboldt, K.D., Dirnagl, U., Villringer,
922 a, Frahm, J., 1996. Simultaneous recording of cerebral blood oxygenation
923 changes during human brain activation by magnetic resonance imaging and
924 near-infrared spectroscopy. J. Cereb. Blood Flow Metab. 16, 817–26.
925 doi:10.1097/00004647-199609000-00006
926 Learmonth, A.E., Newcombe, N.S., Huttenlocher, J., 2001. Toddlers' use of
927 metric information and landmarks to reorient. J. Exp. Child Psychol. 80, 225–
928 244.
929 Li, A., Zhang, Q., Culver, J.P., Miller, E.L., Boas, D. a, 2004. Reconstructing
930 chromosphere concentration images directly by continuous-wave diffuse
931 optical tomography. Opt. Lett. 29, 256–258. doi:10.1364/OL.29.000256
932 Linden, D.E.J., Bittner, R.A., Muckli, L., Waltz, J.A., Kriegeskorte, N., Goebel, R.,
933 Singer, W., Munk, M.H.J., 2003. Cortical capacity constraints for visual
934 working memory: dissociation of fMRI load effects in a fronto-parietal
935 network. Neuroimage 20, 1518–1530.
936 doi:10.1016/j.neuroimage.2003.07.021
937 Liu, H., Boas, D. a, Zhang, Y., Yodh, a G., Chance, B., 1995a. Determination of
938 optical properties and blood oxygenation in tissue using continuous NIR
939 light. Phys. Med. Biol. 40, 1983–1993. doi:10.1088/0031-9155/40/11/015
940 Liu, H., Chance, B., Hielscher, a H., Jacques, S.L., Tittel, F.K., 1995b. Influence
941 of blood vessels on the measurement of hemoglobin oxygenation as
942 determined by time-resolved reflectance spectroscopy. Med. Phys.
943 doi:10.1118/1.597520
944 Logothetis N.K. Augath M., Trinath T., Oeltermann A, P.J., 2001.
945 Neurophysiological investigation of the basis of the fMRI signal. . Nature

412, 150–157.
Luck, S., Vogel, E., 1997. The capacity of visual working memory for features and conjunctions. Nature 390, 279–281.
Luck, S.J., Vogel, E.K., 2013. Visual working memory capacity: from psychophysics and neurobiology to individual differences. Trends Cogn. Sci. 17, 391–400. doi:10.1016/j.tics.2013.06.006
Ma, W.J., Husain, M., Bays, P.M., 2014. Changing concepts of working memory. Nat. Neurosci. 17, 347–356. doi:10.1038/nn.3655
MacIntosh, B.J., Klassen, L.M., Menon, R.S., 2003. Transient hemodynamics during a breath hold challenge in a two part functional imaging study with simultaneous near-infrared spectroscopy in adult humans. Neuroimage 20, 1246–1252. doi:10.1016/S1053-8119(03)00417-8
Maggioni, E., Molteni, E., Zucca, C., Reni, G., Cerutti, S., Triulzi, F.M., Arrigoni, F., Bianchi, A.M., 2015. Investigation of negative BOLD responses in human brain through NIRS technique. A visual stimulation study. Neuroimage 108, 410–422. doi:10.1016/j.neuroimage.2014.12.074
McKendrick, R., Ayaz, H., Olmstead, R., Parasuraman, R., 2014. Enhancing dual-task performance with verbal and spatial working memory training: Continuous monitoring of cerebral hemodynamics with NIRS. Neuroimage 85, 1014–1026. doi:10.1016/j.neuroimage.2013.05.103
Mehagnoul-Schipper, D.J., van der Kallen, B.F.W., Colier, W.N.J.M., van der Sluijs, M.C., van Erning, L.J.T.O., Thijssen, H.O.M., Oeseburg, B., Hoefnagels, W.H.L., Jansen, R.W.M.M., 2002. Simultaneous measurements of cerebral oxygenation changes during brain activation by near-infrared spectroscopy and functional magnetic resonance imaging in healthy young and elderly subjects. Hum. Brain Mapp. 16, 14–23. doi:10.1002/hbm.10026
Molteni, E., Butti, M., Bianchi, A.M., Reni, G., 2008. Activation of the prefrontal cortex during a visual n-back working memory task with varying memory load: a near infrared spectroscopy study. Conf. Proc. IEEE Eng. Med. Biol. Soc. 2008, 4024–7. doi:10.1109/IEMBS.2008.4650092
Munk, M.H.J., Linden, D.E.J., Muckli, L., Lanfermann, H., Zanella, F.E., Singer,

W., Goebel, R., 2002. Distributed cortical systems in visual short-term memory revealed by event-related functional magnetic resonance imaging. Cereb. Cortex 12, 866–876. doi:10.1093/cercor/12.8.866

Murata, Y., Sakatani, K., 2002. Increase in focal concentration of deoxyhaemoglobin during neuronal activity in cerebral ischaemic patients. J. Neurol. … 73, 182–184. doi:10.1136/jnnp.73.2.182

Muthalib, M., Anwar, A.R., Perrey, S., Dat, M., Galka, A., Wolff, S., Heute, U., Deuschl, G., Raethjen, J., Muthuraman, M., 2013. Multimodal integration of fNIRS, fMRI and EEG neuroimaging. Clin. Neurophysiol. 124, 2060–2062. doi:10.1016/j.clinph.2013.03.018

Ogawa, Y., Kotani, K., Jimbo, Y., 2014. Relationship between working memory performance and neural activation measured using near-infrared spectroscopy. Brain Behav. 4, 544–51. doi:10.1002/brb3.238

Okamoto, M., Dan, H., Shimizu, K., Takeo, K., Amita, T., Oda, I., Konishi, I., Sakamoto, K., Isobe, S., Suzuki, T., Kohyama, K., Dan, I., 2004. Multimodal assessment of cortical activation during apple peeling by NIRS and fMRI. Neuroimage 21, 1275–1288. doi:10.1016/j.neuroimage.2003.12.003

Oldendorf WH, I.Y., 1969. Interference of scalp and skull with external measurements of brain isotope content. 1. Isotope content of scalp and skull. J Nucl Med 10:, 177–183.

Perlman, S.B., Huppert, T.J., Luna, B., 2015. Functional Near-Infrared Spectroscopy Evidence for Development of Prefrontal Engagement in Working Memory in Early Through Middle Childhood. Cereb. Cortex 1–10. doi:10.1093/cercor/bhv139

Pessoa, L., Gutierrez, E., Bandettini, P., Ungerleider, L., 2002. Neural correlates of visual working memory: fMRI amplitude predicts task performance. Neuron 35, 975–87.

Pessoa, L., Ungerleider, L.G., 2004. Neural Correlates of Change Detection and Change Blindness in a Working Memory Task — Cereb Cortex. Cereb. Cortex 14, 511–20. doi:10.1093/cercor/bhh013

Pflieger, M.E., Barbour, R.L., 2012. Multimodal Integration of fMRI, EEG, and

NIRS. Biomed. Opt. 3-D Imaging BSu2A.1. doi:10.1364/BIOMED.2012.BSu2A.1

Postle, B.R., 2015. The cognitive neuroscience of visual short-term memory. Curr. Opin. Behav. Sci. 1, 40–46. doi:10.1016/j.cobeha.2014.08.004

Rypma, B., Berger, J.S., D'Esposito, M., 2002. The influence of working-memory demand and subject performance on prefrontal cortical activity. J. Cogn. Neurosci. 14, 721–731. doi:10.1162/08989290260138627

Sakatani, K., Murata, Y., Fujiwara, N., Hoshino, T., Nakamura, S., Kano, T., Katayama, Y., 2013. Comparison of blood-oxygen-level-dependent functional magnetic resonance imaging and near-infrared spectroscopy recording during functional brain activation in patients with stroke and brain tumors. J. Biomed. Opt. 12, 062110. doi:10.1117/1.2823036

Sala, J.B., Courtney, S.M., 2007. Binding of what and where during working memory maintenance. Cortex. 43, 5–21. doi:10.1016/S0010-9452(08)70442-8

Sala, J.B., Rämä, P., Courtney, S.M., 2003. Functional topography of a distributed neural system for spatial and nonspatial information maintenance in working memory. Neuropsychologia 41, 341–356. doi:10.1016/S0028-3932(02)00166-5

Sala-Llonch, R., Peña-Gómez, C., Arenaza-Urquijo, E.M., Vidal-Piñeiro, D., Bargalló, N., Junqué, C., Bartrés-Faz, D., 2012. Brain connectivity during resting state and subsequent working memory task predicts behavioural performance. Cortex 48, 1187–1196. doi:10.1016/j.cortex.2011.07.006

Sassaroli, A., Tonga, Y., Frederickb, B.B., Renshawb, P.F., Ehrenberga, B.L., Fantinia, S., 2005. Studying brain function with concurrent near-infrared spectroscopy (NIRS) and functional magnetic resonance imaging (fMRI). Proc. SPIE 5693, 161–165. doi:10.1117/12.588422

Sato, H., Yahata, N., Funane, T., Takizawa, R., Katura, T., Atsumori, H., Nishimura, Y., Kinoshita, A., Kiguchi, M., Koizumi, H., Fukuda, M., Kasai, K., 2013. A NIRS–fMRI investigation of prefrontal cortex activity during a working memory task. Neuroimage 83, 158–173.

doi:10.1016/j.neuroimage.2013.06.043
Schroeter, M.L., Kupka, T., Mildner, T., Uludağ, K., Von Cramon, D.Y., 2006. Investigating the post-stimulus undershoot of the BOLD signal - A simultaneous fMRI and fNIRS study. Neuroimage 30, 349–358. doi:10.1016/j.neuroimage.2005.09.048
Shafritz, K.M., Gore, J.C., 2002. The role of the parietal cortex in. PNAS 99, 10917–10922.
Siegel, A.M., Culver, J.P., Mandeville, J.B., Boas, D. a, 2003. Temporal comparison of functional brain imaging with diffuse optical tomography and fMRI during rat forepaw stimulation. Phys. Med. Biol. 48, 1391–1403. doi:10.1088/0031-9155/48/10/311
Smith, E.E., Jonides, J., 1998. Neuroimaging analyses of human working memory. Proc. Natl. Acad. Sci. USA 95, 12061–12068. doi:VL - 95
Steinbrink, J., Villringer, A., Kempf, F., Haux, D., Boden, S., Obrig, H., 2006. Illuminating the BOLD signal: combined fMRI-fNIRS studies. Magn. Reson. Imaging 24, 495–505. doi:10.1016/j.mri.2005.12.034
Strangman, G., Culver, J.P., Thompson, J.H., Boas, D. a., 2002. A quantitative comparison of simultaneous BOLD fMRI and NIRS recordings during functional brain activation. Neuroimage 17, 719–731. doi:10.1016/S1053-8119(02)91227-9
Strangman, G.E., Zhang, Q., Li, Z., 2014. Scalp and skull influence on near infrared photon propagation in the Colin27 brain template. Neuroimage 85, 136–149. doi:10.1016/j.neuroimage.2013.04.090
Tachtsidis, I., Scholkmann, F., 2016. False positives and false negatives in functional near-infrared spectroscopy: issues, challenges, and the way forward. Neurophotonics 3, 031405. doi:10.1117/1.NPh.3.3.031405
Tanaka, H., Katura, T., Sato, H., 2014. Task-related oxygenation and cerebral blood volume changes estimated from NIRS signals in motor and cognitive tasks. Neuroimage 94, 107–119. doi:10.1016/j.neuroimage.2014.02.036
Tikhonov A., 1963. Solution of Incorrectly Formulated Problems and the Regularization Method. Sov. Math. Dokl. 5, 1035/1038.

Todd & Marois, R., J.J., 2005. Posterior parietal cortex activity predicts individual differences in visual short-term memory capacity. Cogn. Affect. Behav. Neurosci. 5, 144–155.

Todd, J.J., Fougnie, D., Marois, R., 2005. Visual short-term memory load suppresses temporo-parietal junction activity and induces inattentional blindness. Psychol. Sci. 16, 965–72. doi:10.1111/j.1467-9280.2005.01645.x

Todd, J.J., Marois, R., 2004. Capacity limit of visual short-term memory in human posterior parietal cortex. Nature 428, 751–754.

Tong, Y., Frederick, B. deB, 2012. Concurrent fNIRS and fMRI processing allows independent visualization of the propagation of pressure waves and bulk blood flow in the cerebral vasculature. Neuroimage 61, 1419–1427. doi:10.1016/j.neuroimage.2012.03.009

Toronov, V., Webb, a, Choi, J.H., Wolf, M., Michalos, a, Gratton, E., Hueber, D., 2001. Investigation of human brain hemodynamics by simultaneous near-infrared spectroscopy and functional magnetic resonance imaging. Med. Phys. 28, 521–527. doi:10.1118/1.1354627

Tsujimoto, S., Yamamoto, T., Kawaguchi, H., Koizumi, H., Sawaguchi, T., 2004. Prefrontal cortical activation associated with working memory in adults and preschool children: An event-related optical topography study. Cereb. Cortex. doi:10.1093/cercor/bhh030

Tsuzuki, D., Dan, I., 2014. Spatial registration for functional near-infrared spectroscopy: From channel position on the scalp to cortical location in individual and group analyses. Neuroimage. doi:10.1016/j.neuroimage.2013.07.025

Wijeakumar, S., Shahani, U., McCulloch, D.L., Simpson, W. a., 2012a. Neural and vascular responses to fused binocular stimuli: A VEP and fNIRS study. Investig. Ophthalmol. Vis. Sci. 53, 5881–5889. doi:10.1167/iovs.12-10399

Wijeakumar, S., Shahani, U., Simpson, W. a., McCulloch, D.L., 2012b. Localization of hemodynamic responses to simple visual stimulation: An fNIRS study. Investig. Ophthalmol. Vis. Sci. 53, 2266–2273. doi:10.1167/iovs.11-8680

Wijeakumar, S., Spencer, J.P., Bohache, K.P., Boas, D.A., Magnotta, V.A., 2015. Validating a new methodology for optical probe design and image registration in fNIRS studies. Neuroimage 106, 86–100.

Xu, Y., Chun, M.M., 2006. Dissociable neural mechanisms supporting visual short-term memory for objects. Nature 440, 91–5. doi:10.1038/nature04262

Yamamoto, T., Kato, T., 2002. Paradoxical correlation between signal in functional magnetic resonance imaging and deoxygenated haemoglobin content in capillaries: a new theoretical. Phys. Med. Biol. 47, 1121–1141. doi:10.1088/0031-9155/47/7/309

Yücel, M. a, Selb, J., Cooper, R.J., Boas, D. a, 2014. Targeted Principle Component Analysis: A new motion artifact correction approach for near-infrared spectroscopy. J. Innov. Opt. Health Sci. 7, 1–8. doi:10.1142/S1793545813500661

Yücel, M. a., Huppert, T.J., Boas, D. a., Gagnon, L., 2012. Calibrating the BOLD signal during a motor task using an extended fusion model incorporating DOT, BOLD and ASL data. Neuroimage 61, 1268–1276. doi:10.1016/j.neuroimage.2012.04.036

Zhang, X., Noah, J.A., Hirsch, J., 2016. Separation of the global and local components in functional near-infrared spectroscopy signals using principal component spatial filtering. Neurophotonics 3, 015004. doi:10.1117/1.NPh.3.1.015004

Supplementary Material

T1. Number of voxels showing significant positive and negative HbO and HbR correlations with BOLD for each of the 12 conditions.

	Number of voxels			
	Positive HbO-BOLD	**Positive HbR-BOLD**	**Negative HbO-BOLD**	**Negative HbR-BOLD**
CR2	360	549	574	516
CR4	389	432	670	309
CR6	494	443	630	438
FA2	490	754	629	69
FA4	483	462	253	248
FA6	239	402	730	336
Hit2	756	782	482	924
Hit4	764	924	294	287
Hit6	304	313	428	551
Miss2	291	436	438	503
Miss4	195	776	370	383
Miss6	343	362	208	263

T2. Regions that showed a positive correlation between BOLD and HbO concentration for Hit4 trials. Exemplar clusters from tis table have been shown in Figure 7.

Region	**Hemi**	**Peak voxel MNI Coordinates (LPI orientation)**			**Size (mm^3)**	**Peak voxel R value**
		x	**y**	**z**		
Superior parietal lobule	R	28	-80	52	1400	0.9737
Superior parietal lobule	R	18	-86	50	520	0.9752
Inferior parietal lobule	L	-60	-50	36	400	0.8538
Supramarginal gyrus	L	-70	-26	18	1096	0.9955
Postcentral gyrus	R	62	-8	32	312	0.7805
Superior temporal gyrus	R	70	-16	2	280	0.9679
Superior temporal gyrus	R	64	-26	12	520	0.8855
Middle frontal gyrus	R	40	24	48	304	0.7541
Middle frontal gyrus	L	-44	46	20	288	0.8373
Superior frontal gyrus	R	20	60	22	712	0.8696
Cuneus	R	6	-86	42	280	0.7802

T3. Regions that showed a positive correlation between BOLD and HbR concentration for Hit4 trials.

Region	Hemi	Peak voxel MNI Coordinates (LPI orientation)			Size (mm^3)	Peak voxel R value
		x	y	z		
Superior parietal lobule	R	18	-86	50	992	0.9821
Superior parietal lobule	R	24	-64	60	352	0.8273
Superior parietal lobule	L	-26	-84	46	272	0.841
Inferior parietal lobule	L	-48	-56	54	256	0.8925
Supramarginal gyrus	L	-70	-26	18	224	0.9523
Superior temporal gyrus	R	58	-20	4	648	0.7788
Middle frontal gyrus	L	-44	44	22	840	0.883
Middle frontal gyrus	R	42	24	48	392	0.7519
Inferior frontal gyrus	R	54	30	22	576	0.8567
Inferior frontal gyrus	L	-40	36	0	544	0.7456
Inferior frontal gyrus	L	-38	10	28	400	0.7788
Inferior frontal gyrus	R	48	38	12	88	0.7159
Superior frontal gyrus	R	22	58	24	752	0.8886
Superior frontal gyrus	R	20	56	10	240	0.7837
Superior frontal gyrus	R	26	58	18	240	0.7852
Superior occipital gyrus	R	20	-78	36	352	0.8394
Cuneus	L	6	-82	42	224	0.7637

T4. Regions that showed a positive correlation between BOLD and HbO concentration for CR4 trials. Exemplar clusters from tis table have been shown in Figure 8.

Region	Hemi	Peak voxel MNI Coordinates (LPI orientation)			Size (mm^3)	Peak voxel R value
		x	y	z		
Superior parietal lobule	R	18	-86	50	696	0.9719
Superior parietal lobule	R	26	-80	52	632	0.9501
Inferior parietal lobule	L	-50	-50	46	384	0.8477
Postcentral gyrus	R	64	-6	30	632	0.8839
Superior temporal gyrus	L	-60	-34	14	768	0.8242

T5. Regions that showed a positive correlation between BOLD and HbR concentration for CR4 trials.

Region	Hemi	Peak voxel MNI Coordinates (LPI orientation)			Size (mm^3)	Peak voxel R value
		x	y	z		
Inferior parietal lobule	L	-56	-54	42	456	0.8515
Superior parietal lobule	R	18	-86	50	224	0.9633
Postcentral gyrus	R	58	-8	30	24	0.624
Middle frontal gyrus	R	48	42	10	1032	0.8716
Middle frontal gyrus	L	-40	48	20	456	0.8656
Inferior frontal gyrus	R	52	28	20	640	0.9065
Superior frontal gyrus	R	18	58	22	544	0.8267
Cuneus	R	6	-82	44	80	0.7926

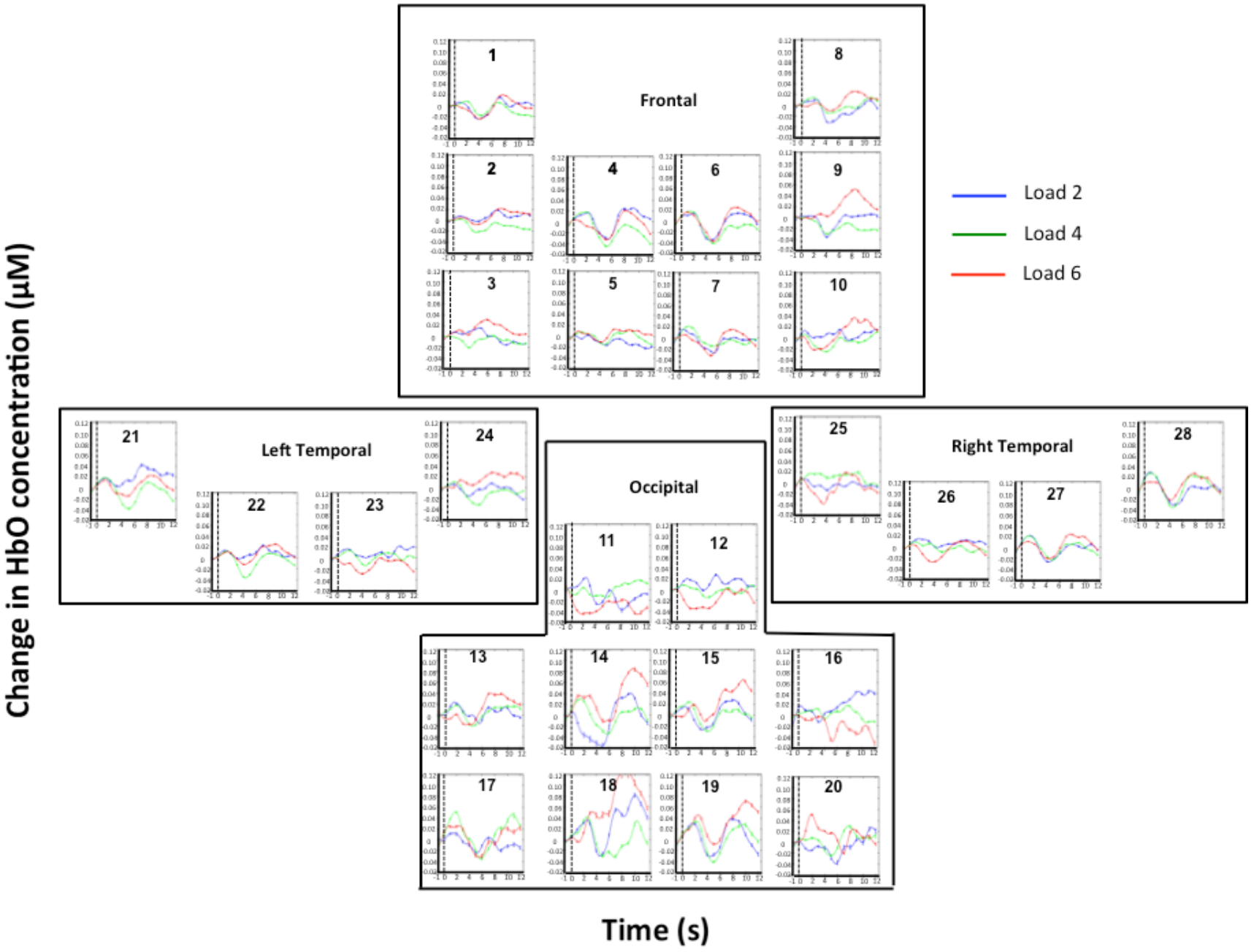
Change in HbO concentration (μM)
Frontal
Left Temporal
Occipital
Right Temporal
Load 2
Load 4
Load 6
Time (s)

F2. Weighted block average HbO signals for Hit trials for Loads 2 (shown in blue),4 (shown in green) and 6 (shown in red) across the frontal (outlined in red), temporal (outlined in green) and parietal (outlines in blue) channels. Figure shown for illustration purposes. Note that GLM analyses were used for the image-reconstruction approach (see text for details). Dotted line indicates the onset of the sample array.

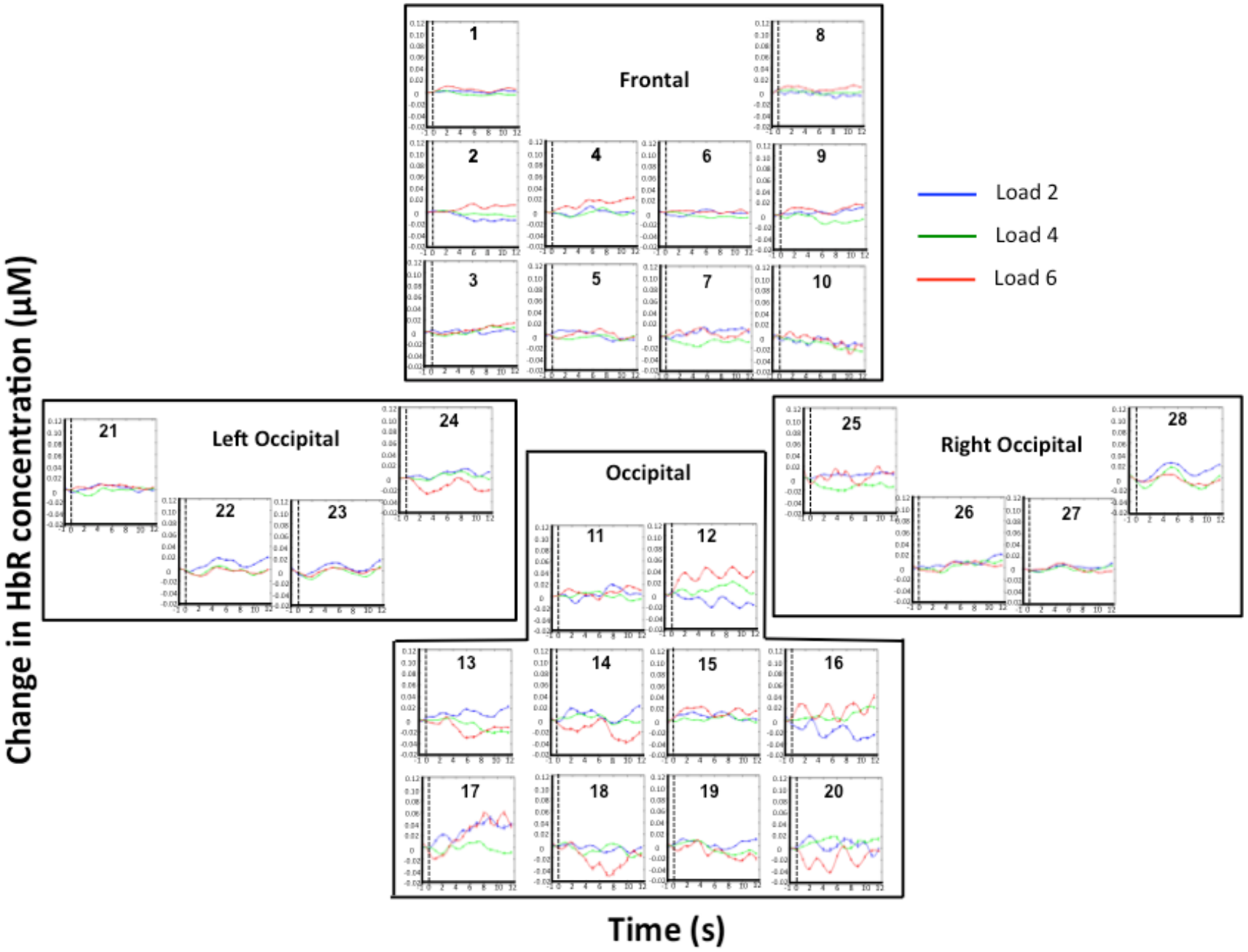
Frontal
1
2
3
4
5
6
7
8
9
10
Load 2
Load 4
Load 6
Left Occipital
21
22
23
24
Occipital
11
12
13
14
15
16
17
18
19
20
Right Occipital
25
26
27
28
Change in HbR concentration (µM)
Time (s)

F3. Weighted block average HbR signals for Hit trials for Loads 2 (shown in blue),4 (shown in green) and 6 (shown in red) across the frontal (outlined in red), temporal (outlined in green) and parietal (outlines in blue) channels. Figure shown for illustration purposes. Note that GLM analyses were used for the image-reconstruction approach (see text for details). Dotted line indicates the onset of the sample array.

1164